



Prediction of drug efficacy from transcriptional profiles with deep learning

Jie Zhu^{1,2,6}, Jingxiang Wang^{3,6}, Xin Wang^{2,6}, Mingjing Gao^{3,6}, Bingbing Guo^{4,6}, MiaoMiao Gao¹, Jiarui Liu⁴, Yanqiu Yu¹, Liang Wang², Weikaixin Kong^{1D}⁵, Yongpan An², Zurui Liu³, Xinpei Sun^{1D}¹, Zhuo Huang^{1D}⁵, Hong Zhou^{2,7}✉, Ning Zhang^{1,7}✉, Ruimao Zheng^{4,7}✉ and Zhengwei Xie^{1,3,7}✉

Drug discovery focused on target proteins has been a successful strategy, but many diseases and biological processes lack obvious targets to enable such approaches. Here, to overcome this challenge, we describe a deep learning-based efficacy prediction system (DLEPS) that identifies drug candidates using a change in the gene expression profile in the diseased state as input. DLEPS was trained using chemically induced changes in transcriptional profiles from the L1000 project. We found that the changes in transcriptional profiles for previously unexamined molecules were predicted with a Pearson correlation coefficient of 0.74. We examined three disorders and experimentally tested the top drug candidates in mouse disease models. Validation showed that perillen, chikusetsusaponin IV and trametinib confer disease-relevant impacts against obesity, hyperuricemia and nonalcoholic steatohepatitis, respectively. DLEPS can generate insights into pathogenic mechanisms, and we demonstrate that the MEK-ERK signaling pathway is a target for developing agents against nonalcoholic steatohepatitis. Our findings suggest that DLEPS is an effective tool for drug repurposing and discovery.

Recent developments in the application of deep learning to diverse areas (for example, natural language processing, computer vision and so on) suggest the potential of advanced algorithms for the assessment of chemicals in applications such as molecular encoding, chemical synthesis route planning and inhibitor target prediction^{1–5}. Combined with resources developed in computational chemistry, these deep learning tools are changing the landscape of chemical and pharmaceutical research and development (for example, enabling rapid sampling of a vast chemical space and allowing researchers to make accurate predictions about structure–function relationships).

Drug development based on target proteins has been a successful approach in the past decades, but these methods cannot address diseases that lack well-defined protein targets. One strategy for developing drugs to treat these diseases would be to generate a model capable of predicting efficacy independent of specific targets. A recent study showed how a new antibiotic candidate for treating *Escherichia coli* infections was found using a customized deep learning model⁶. However, this kind of model is built on a case-by-case basis and relies on phenotypic data specific to a single disease state; that is, it lacks the ability to generalize to other diseases.

Given that most diseases are associated with characteristic changes in gene expression profiles, such changes are used as indicators reflecting the underlying mechanisms of diseases, an assumption embodied in the Connectivity Map (CMap) concept^{7–10}. However, CMap is applicable only to the molecules whose transcriptional profiles have already been experimentally assessed. We envisioned that a model capable of predicting chemically inducible

changes in transcriptional profiles (CTPs) for an unlimited number of small molecules would make it much easier to find potent agents to develop as treatments for most diseases. First, we constructed a neural network using simplified molecular-input line-entry system (SMILES) chemical encoding as input to fit CTPs that were measured in the L1000 project¹¹ (Fig. 1a). Second, using gene signatures specific to pathological contexts, we employed gene set enrichment analysis (GSEA)¹² to evaluate the potential efficacy of compounds against these diseases. We refer to this approach and model as DLEPS.

Results

The architecture and training of DLEPS. To build a general-purpose model that is suitable for use with many diseases, especially for disorders without well-defined targets, we developed DLEPS comprising two stages. First, we trained a deep neural network to predict CTPs based on data from cell culture screening with diverse compounds (Fig. 1a). The SMILES encoding of small molecules was initially parsed to a grammar tree¹³, which was then encoded to a point randomly in a high-dimensional sphere (Fig. 1a, middle). The latent vector was further passed to a deep dense network to predict the CTPs (Fig. 1a, right).

Second, we selected upregulated and downregulated gene signatures that should reflect pathological changes in gene expression levels; here, we employed GSEA, which has been adopted in CMap, to compute an enrichment score as the efficacy score^{7,9}. According to this score, we finally selected several top-ranked candidate small molecules to be assayed with cell cultures or directly in animal models

¹Peking University International Cancer Institute, Health Science Center, Peking University, Beijing, China. ²Department of Pharmacology, School of Basic Medical Sciences, Health Science Center, Peking University, Beijing, China. ³Beijing & Qingdao Langu Pharmaceutical R&D Platform, Beijing Gigaceuticals Tech. Co. Ltd., Beijing, China. ⁴Department of Anatomy, Histology and Embryology, Neuroscience Research Institute, Health Science Center, Peking University, Beijing, China. ⁵State Key Laboratory of Natural and Biomimetic Drugs, School of Pharmaceutical Sciences, Health Science Center, Peking University, Beijing, China. ⁶These authors contributed equally: Jie Zhu, Jingxiang Wang, Xin Wang, Mingjing Gao, Bingbing Guo. ⁷These authors jointly supervised this work: Hong Zhou, Ning Zhang, Ruimao Zheng, Zhengwei Xie. ✉e-mail: rainbow_zhou@126.com; zhangning@bjmu.edu.cn; rmzheng@pku.edu.cn; xiezhengwei@hsc.pku.edu.cn

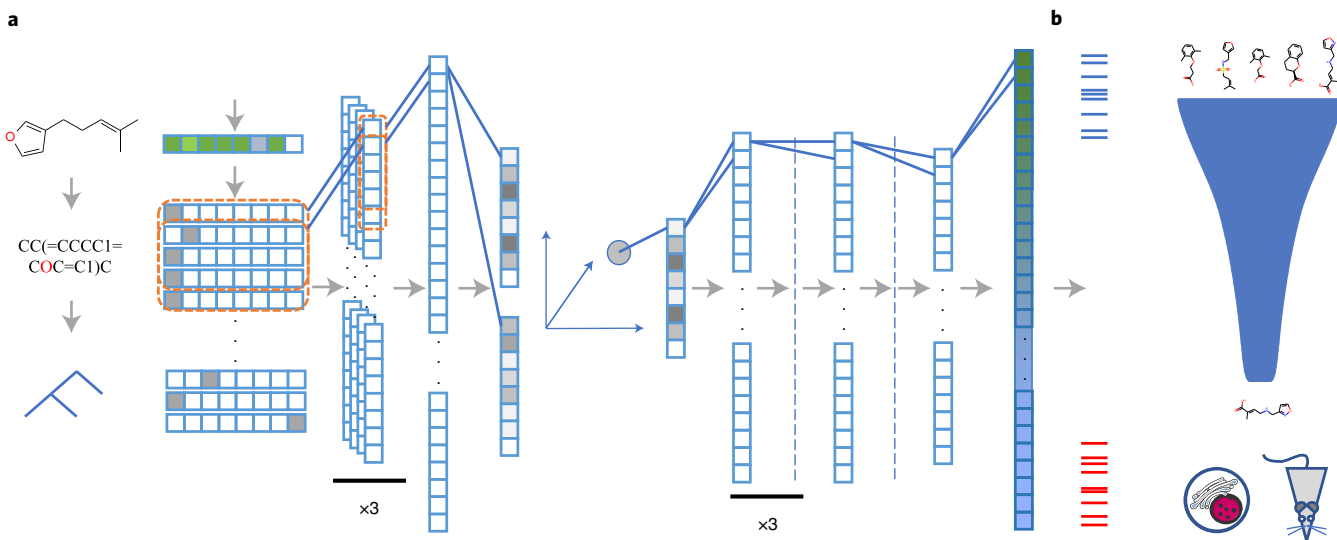


Fig. 1 | A schematic representation of the deep learning model underlying DLEPS. **a**, The molecules were first represented by SMILES, then parsed to a grammar tree, and then to a one-hot array, which was then passed to three layers of one-dimensional convolutional neural networks. The output slices were flattened and then passed to a dense layer, which output the mean vector and radius vector to encode a sphere in high-dimensional space. The coordinates of a randomly sampled point in this sphere were chosen as the latent vector, which was then passed through a five-layer dense network (dashed line indicates a dropout layer) for prediction of CTPs of 978 landmark genes. Finally, the 978 landmark genes were converted to 12,328 genes through linear transformation (see Methods for details of all layers). **b**, Gene signatures of particular diseases of interest were employed to predict the efficacy of compounds using GSEA. Then virtual screening was performed against the selected chemical library. Efficacy was tested using cell lines or animal models directly, rather than through initial testing at the protein level.

(Fig. 1b). Corresponding to the two stages of our model, our system requires two input types: a selected chemical library; and a gene set (for example, GSEA gene signature(s) or top-ranking differentially expressed gene (DEG) lists).

We employed high-throughput screening data from the L1000 project to initially fit the model. L1000 covers transcriptional changes induced by 20,000 small molecules¹¹. Analysis of Chemistry Development Kit (CDK) fingerprints using *t*-distributed stochastic neighbor embedding (*t*-SNE) showed that the molecules were clustered into about 50 groups (Fig. 2a). As expected, the molecules induced varying numbers of genes (see Supplementary Information for further analysis (related to Extended Data Fig. 1a–f), Fig. 2b and Extended Data Fig. 2a). After filtering, 17,051 molecules were randomly split to generate a training set (14,051), a validation set (1,500) and a test set (1,500; Fig. 2c).

Next, upon combining suitable preprocessing steps and hyperparameters (see Methods), the model converged rapidly during training (Fig. 2d). The CTPs (quantified as *z* scores) from both the training and test sets were extremely well fitted (scatter plots are shown in Fig. 2e,h), with areas under the curve (AUC) for correlation coefficient cut (receiver operating characteristic (ROC)-like) curves around 0.90 and 0.74, respectively (Fig. 1f,g,i,j).

Two features of DLEPS need to be emphasized. First, DLEPS is capable of predicting the CTP-associated activity of novel scaffold/structures of small molecules or chemical compounds (Extended Data Fig. 2a–d). Second, DLEPS is able to distinguish the CTP-associated activities of highly similar molecule pairs, even when these molecules differ in one chemical group (Extended Data Fig. 2e–k). See the Supplementary Information for details (related to Extended Data Fig. 2a–k and Supplementary Table 1). In the following sections, we describe the application of DLEPS with variable gene signatures and library selection.

Seeking anti-obesity molecules using browning gene signatures.

Having trained DLEPS to simulate experimental measurements of

CTPs, our first application sought to identify novel therapeutics for the treatment of obesity. Given that brown fat cells are able to dissipate energy and thus counteract obesity^{14,15}, we used an unbiased set of 150 up/downregulated genes from comparison of brown adipose tissue versus white adipose tissue (WAT) from 3 male C57BL/6 mice¹⁵ as the GSEA gene signature input to calculate an omics score (*b* – *a*, see Methods); we also prepared an ‘expert score’ based on 20 browning genes and 9 whitening genes that were curated by adipose tissue experts. All genes were mapped to human genes prior to use with DLEPS.

For the user-defined library, we here chose the rapid drug development D3680 library, which comprises 961 drugs approved by the Food and Drug Administration (FDA) and 2,719 natural compounds (Supplementary Table 2). The omics score and expert score were plotted (Fig. 3a) and visualized with a *t*-SNE plot of the CDK fingerprints for all of the molecules in the library (Fig. 3b). Note that these compounds were not included in the training set. Ultimately, four natural products positioned at the upper right corner (rank < 150 for both scores) were chosen as the candidate set and four other compounds were chosen as a negative set; these were assessed experimentally.

We examined the pharmacological effects of the selected molecules on obesity prevention by initially performing intraperitoneal (i.p.) administration of isoginkgetin (I, 3 mg per kilogram of body weight (3 mg kg^{-1})), chelidonine (20 mg kg^{-1}), loureirin B (L, 1 mg kg^{-1}) and chikusetsusaponin IV (C, 20 mg kg^{-1}) to diet-induced obesity model mice⁹ (given a high-fat diet (HFD) fed daily for 14 days). We found that I/L/C each caused significant reductions in the rate of body weight gain compared with vehicle treatment ($P < 0.01$; Fig. 3c and Extended Data Fig. 3a), while four negatively predicted compounds had no reductive effect (Extended Data Fig. 3g–i). Note that a longer (5 week) study showed that chikusetsusaponin IV treatment conferred a 21% reduction (Extended Data Fig. 3b). Moreover, we found that I/L/C treatments did not affect the food intake (Extended Data Fig. 3c,d) or the daily locomotor activity of the

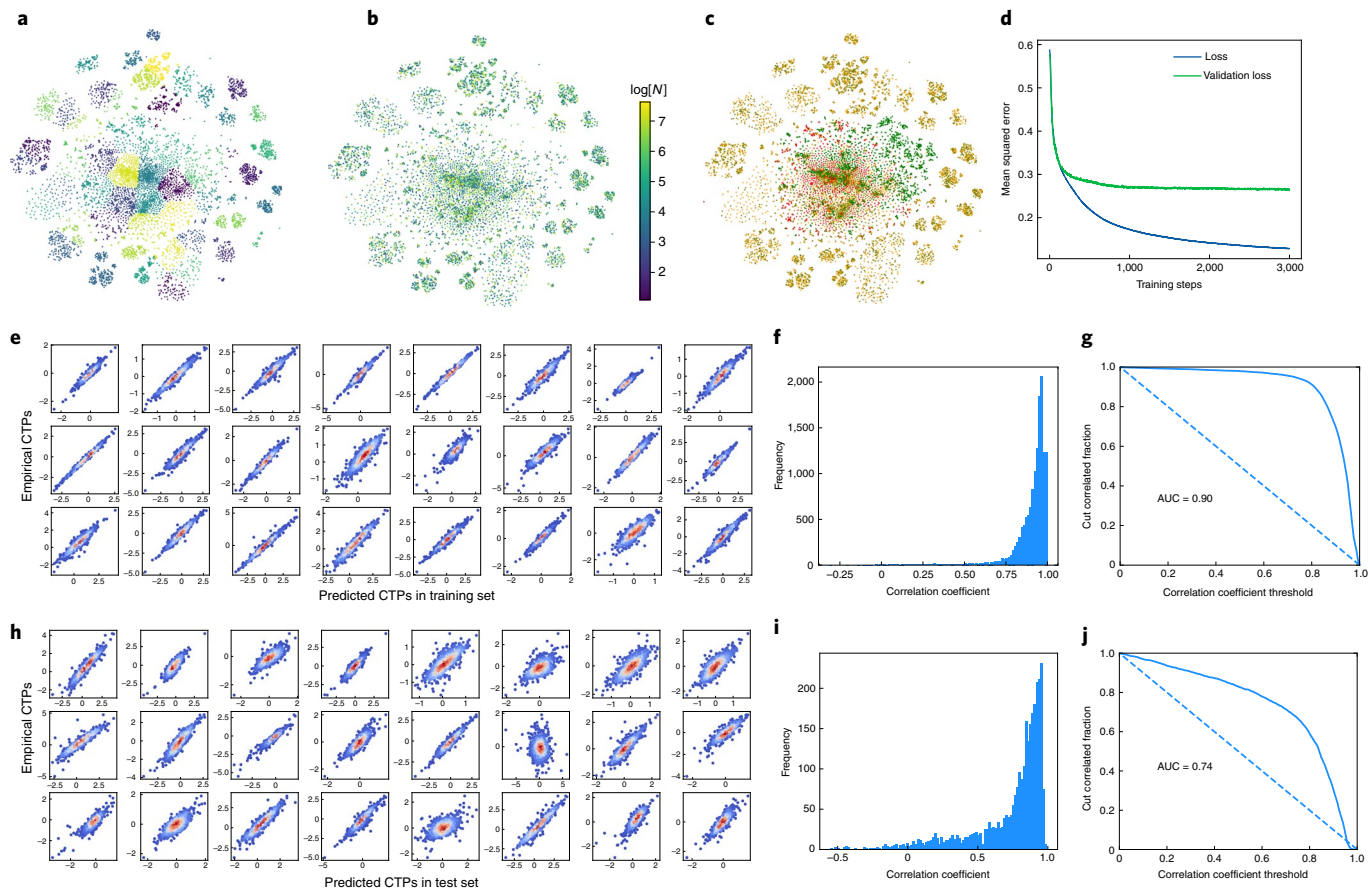


Fig. 2 | Training results of the deep learning model underlying DLEPS. **a**, t-SNE analysis of the CDK fingerprints of all of the small molecules used (including the training and test sets), showing their structural diversity. **b**, The number of changed genes for each molecule is colored in a log scale. **c**, The data were split into a training set (14,051 molecules; olive) and a validation/test set (3,000 molecules; orange). The FDA-approved drugs and natural products for virtual screening are marked in red and green, respectively. For clarity, data points in **a,b** use the same coordinates in **c**. **d**, The mean squared error loss of training and validation loss in the first 3,000 steps. **e,h**, Scatter plots of the empirical data versus the predicted data in the training (**e**) and test (**h**) datasets. The color gradient indicates the dot intensity. **f,i**, The distribution of Pearson correlation coefficient r values in the training (**f**) and test (**i**) datasets. **g,j**, The ROC-like curve of the well-fitted fraction versus the threshold Pearson r in the training (**g**) and test (**j**) datasets.

mice (Extended Data Fig. 3e,f). We further observed that the I/L/C treatments markedly reduced the weights of the inguinal and epididymal fat pads of the diet-induced obesity model mice (Fig. 3d,e), induced canonical adipose browning phenotypes (Fig. 3f), leading to enhanced oxygen consumption (\dot{V}_{O_2}) and carbon dioxide production (\dot{V}_{CO_2}), elevated whole-body energy expenditure (EE) and decreased respiratory exchange ratio (RER; Fig. 3g–j).

We further examined the expression levels of the genes comprising the browning gene signatures in inguinal WAT (iWAT) of these mice; I/L/C treatments each markedly increased the expression levels of genes known to function in adipose browning induction and adaptive thermogenesis (Fig. 3k,l). Note that these genes were used to calculate the expert score. These results established that the I/L/C treatments each effectively promoted WAT browning. Thus, our initial application of DLEPS in obesity resulted in a successful proof-of-concept demonstration, identifying a set of three natural product compounds that should now be understood as new candidates for the development of anti-obesity therapies.

Identification of anti-hyperuricemia molecules using multiple gene signatures. Having demonstrated that DLEPS worked very well with obesity-related gene signatures as input, we next extended its application using gene signatures for diverse aspects of a chronic metabolic disorder known as hyperuricemia (HUA)^{16,17}.

The development of HUA is often associated with inflammation and renal fibrosis¹⁸. We therefore assumed it would be beneficial if we targeted both HUA per se and inflammation/fibrosis, so we calculated a HUA score and an inflammation/fibrosis score using their corresponding gene signatures^{19–21} as inputs (see Methods). Again, using the D3680 library as input, we ultimately selected a set of four candidate natural compounds and drugs from the upper right corner that were common to both the HUA score (top 1%) and inflammation/fibrosis score (top 16%) DLEPS outputs (red dots in Fig. 4a,b). We also selected four molecules from the lower bottom corner as a negative set (green dots in Fig. 4a,b).

Experiments with the HUA model mice revealed that perillen, lobetiolin and deacetyltaxol (20 mg kg⁻¹ d⁻¹ for all compounds) each lowered the blood uric acid level (Fig. 4c). None of the molecules from the negative set affected uric acid levels (Extended Data Fig. 4a). We conducted further studies in which we compared perillen—a natural product obtained from the traditional Chinese herbal plant *Perilla frutescens*^{22,23}—against four HUA drugs already on the market. All of these drugs were administered at a dose of 20 mg kg⁻¹ d⁻¹, and we found that perillen exerted a superior effect in lowering blood uric acid levels compared with benzboromarone and had similar efficacy to the three other drugs (Fig. 4d). We found that perillen lowered serum uric acid levels in a dose-dependent manner (Fig. 4e), and also noted that perillen

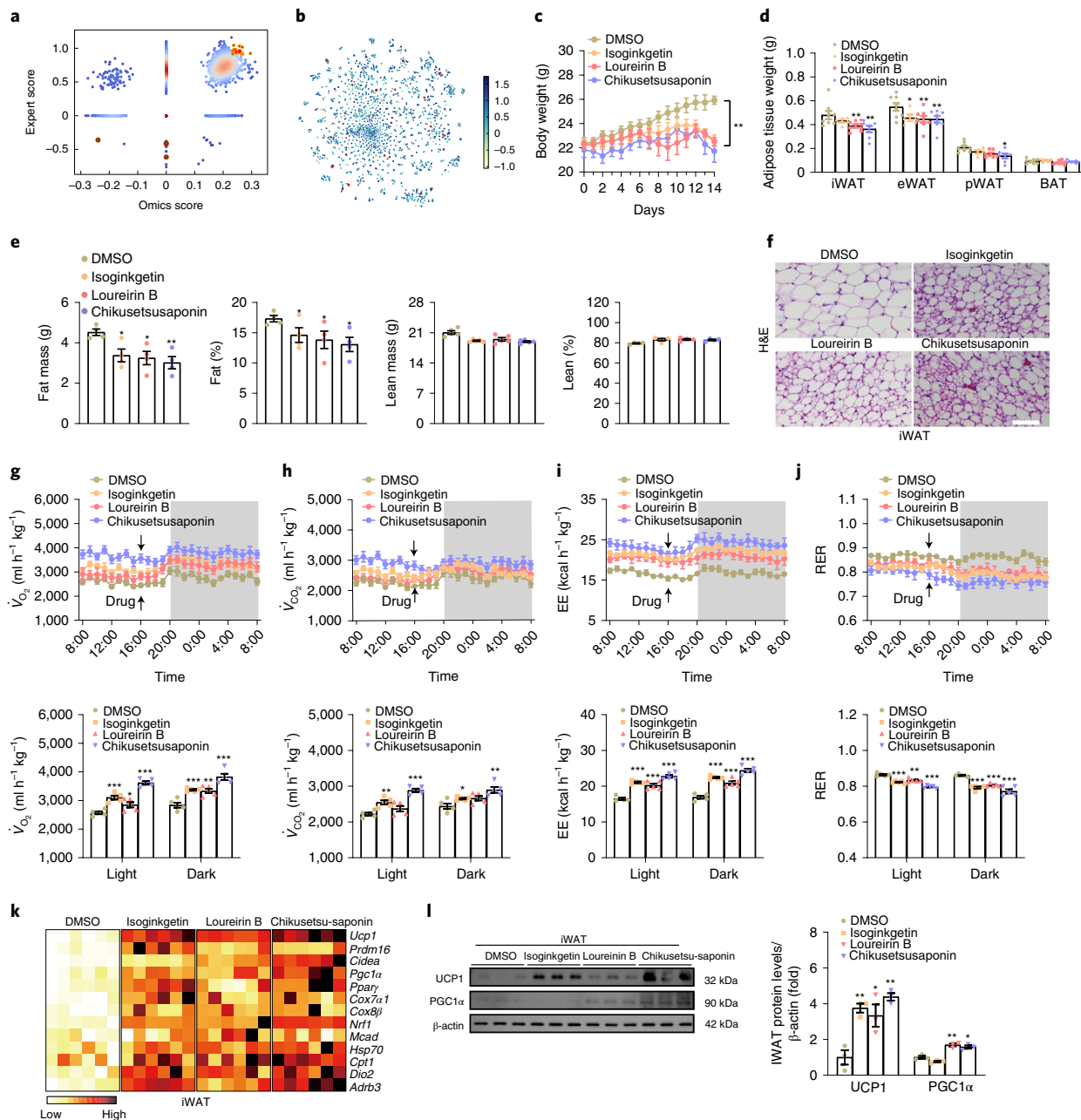


Fig. 3 | The DLEPS-identified candidate anti-obesity molecules I/L/C promote WAT browning, elevate EE and prevent diet-induced obesity. **a**, A scatter plot of the expert score (*b* - *a*) versus the omics score (*b* - *a*). The computationally predicted obesity-treatment candidate molecules highlighted in red were selected for experimental follow up. The color gradient shows the density of the dots. **b**, t-SNE analysis of the CDK fingerprints of the D3680 molecules. **c-e**, 8-week-old mice were housed at 22 °C, fed a HFD and treated with isoginkgetin (3 mg kg⁻¹), loureirin B (1 mg kg⁻¹), chikusetsusaponin IV (20 mg kg⁻¹) or dimethylsulfoxide (DMSO) control for 2 weeks. **c**, Body weight (*n* = 6 for each group). **d**, Adipose tissue weight (*n* = 8 in the DMSO and loureirin groups, *n* = 7 in the chikusetsusaponin IV group, *n* = 5 in the isoginkgetin group). The *P* values of iWAT (epididymal WAT (eWAT), retroperitoneal WAT (pWAT) and brown adipose tissue (BAT)) in the I/L/C groups compared with the DMSO group are 0.166 (0.011, 0.310 and 0.826), 0.003 (0.001, 0.090 and 0.703) and 0.001 (0.003, 0.040 and 0.909), respectively. **e**, Left: fat mass and fat percentage; right: lean mass and lean percentage (*n* = 4 for each group). The *P* values of fat mass (fat mass percentage, lean mass and lean mass percentage) in the I/L/C groups compared with the DMSO group are 0.018 (0.023, 0.072 and 0.110), 0.013 (0.046, 0.109 and 0.051) and 0.004 (0.017, 0.057 and 0.075), respectively. **f**, Hematoxylin and eosin (H&E) staining (3 mouse replicates). Scale bar, 20 μm. **g-j**, Indirect calorimetry was performed to quantify \dot{V}_{O_2} (**g**), \dot{V}_{CO_2} (**h**), EE (**i**) and RER (**j**) of I/L/C- or DMSO-treated mice during complete 24 h light-dark cycles; the arrow indicates the time of i.p. injection (**g-j**, *n* = 5 for each group). The *P* values of \dot{V}_{O_2} (\dot{V}_{CO_2} and EE/RER) in the I/L/C groups compared with the DMSO group are 0.001 (0.002 and 0.001), 0.029 (0.126 and 0.001) and 0.001 (0.001 and 0.001), under light conditions, respectively. The *P* values of \dot{V}_{O_2} (\dot{V}_{CO_2} and EE/RER) in the I/L/C groups compared with the DMSO group are 0.001 (0.001 and 0.001), 0.003 (0.003 and 0.003) and 0.001 (0.001 and 0.001), under dark conditions, respectively. **k**, A heatmap visualization of the relative mRNA expression of known browning-associated genes in iWAT (*n* = 6 for each group). **l**, Western blotting for quantification of UCP1 and PGC1α protein levels in iWAT (3 replicates); the *P* values of UCP1 (PGC1α) in the I/L/C groups compared with the DMSO group are 0.004 (0.066), 0.035 (0.004) and 0.001 (0.010), respectively. The values are expressed as the mean ± s.e.m. All *P* values were determined by one-way analysis of variance. **P* < 0.05, ***P* < 0.01, ****P* < 0.001 compared with the model group. All data are presented as the mean ± s.e.m.

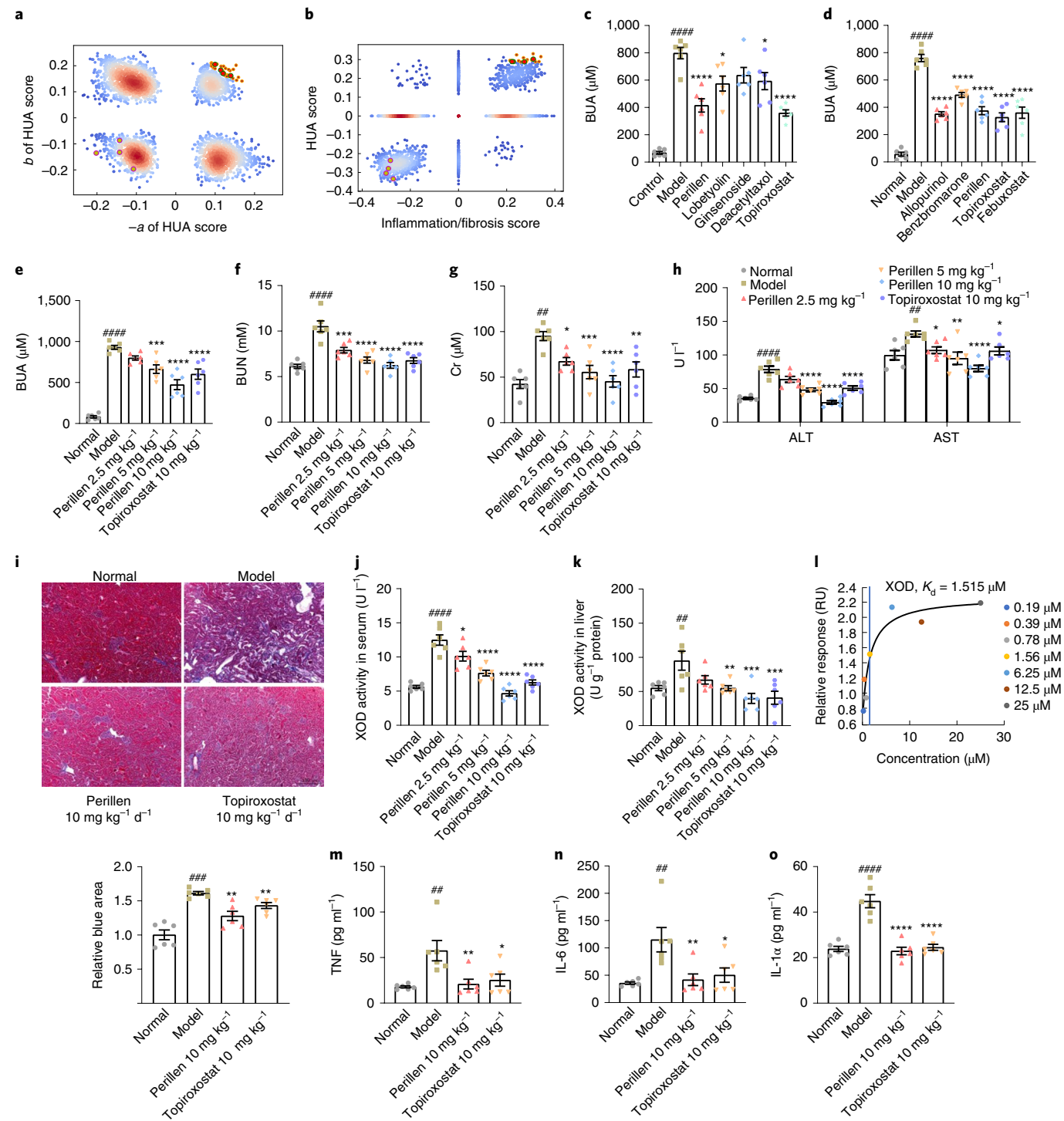


Fig. 4 | The DLEPS-predicted anti-HUA natural compound perillen lowers blood uric acid levels in HUA model mice. **a**, A scatter plot of enrichment scores b versus $-a$ from DLEPS based on only HUA gene signatures as the genetic input. The red dots indicate $(b - a) > 0.2875$. **b**, A scatter plot of the HUA score ($b - a$) versus the inflammation/fibrosis score ($b - a$). Molecules selected for experimental evaluation are highlighted in red (for positive set) or green (negative set). **c,d**, Blood uric acid (BUA) levels of control, HUA model mice (induced with oxonate and hypoxanthine) and HUA model mice treated with four DLEPS-predicted molecules (perillen, lobetyolin, ginsenoside compound K and deacetyltaxol at 20 mg kg⁻¹ d⁻¹, using topiroxostat at 20 mg kg⁻¹ d⁻¹ as a positive control; **c**) and comparison of perillen with the four indicated FDA-approved anti-HUA drugs (20 mg kg⁻¹ d⁻¹, 7 days, **d**). **e-h**, BUA levels (**e**), BUN (**f**), serum creatinine (Cr, **g**) and ALT/AST (**h**) levels of normal mice, induced HUA model mice and perillen-treated HUA model mice, as well as HUA model mice treated with the known anti-HUA drug topiroxostat. (**c-h**, $n=6$ for each group.) **i**, Masson trichrome staining of the kidney tissues of the normal, model, perillen (10 mg kg⁻¹ d⁻¹)-treated and topiroxostat (10 mg kg⁻¹ d⁻¹)-treated mice (3 mouse replicates). Bottom panel, quantification of fibrosis in top panels. **j,k**, XOD activity in serum (**j**) and liver (**k**) of normal, induced HUA model, perillen-treated (2.5, 5 and 10 mg kg⁻¹ doses) and topiroxostat-treated ($n=6$ for each group) mice. **l**, The in vitro binding affinity of perillen with XOD, assayed via SPR using a Biacore 3000 instrument. **m-o**, Levels of tumor necrosis factor (TNF, **m**), interleukin-6 (IL-6, **n**) and IL-1 β (**o**) in normal, HUA model, perillen-treated and topiroxostat-treated mice ($n=6$ for each group). * $P < 0.05$, ** $P < 0.01$, *** $P < 0.001$, **** $P < 0.0001$ compared with the model group. ## $P < 0.01$, ### $P < 0.001$, ##### $P < 0.0001$ compared with the normal group. All P values were determined by Student's t -test (two-tailed). All data are presented as the mean \pm s.e.m.

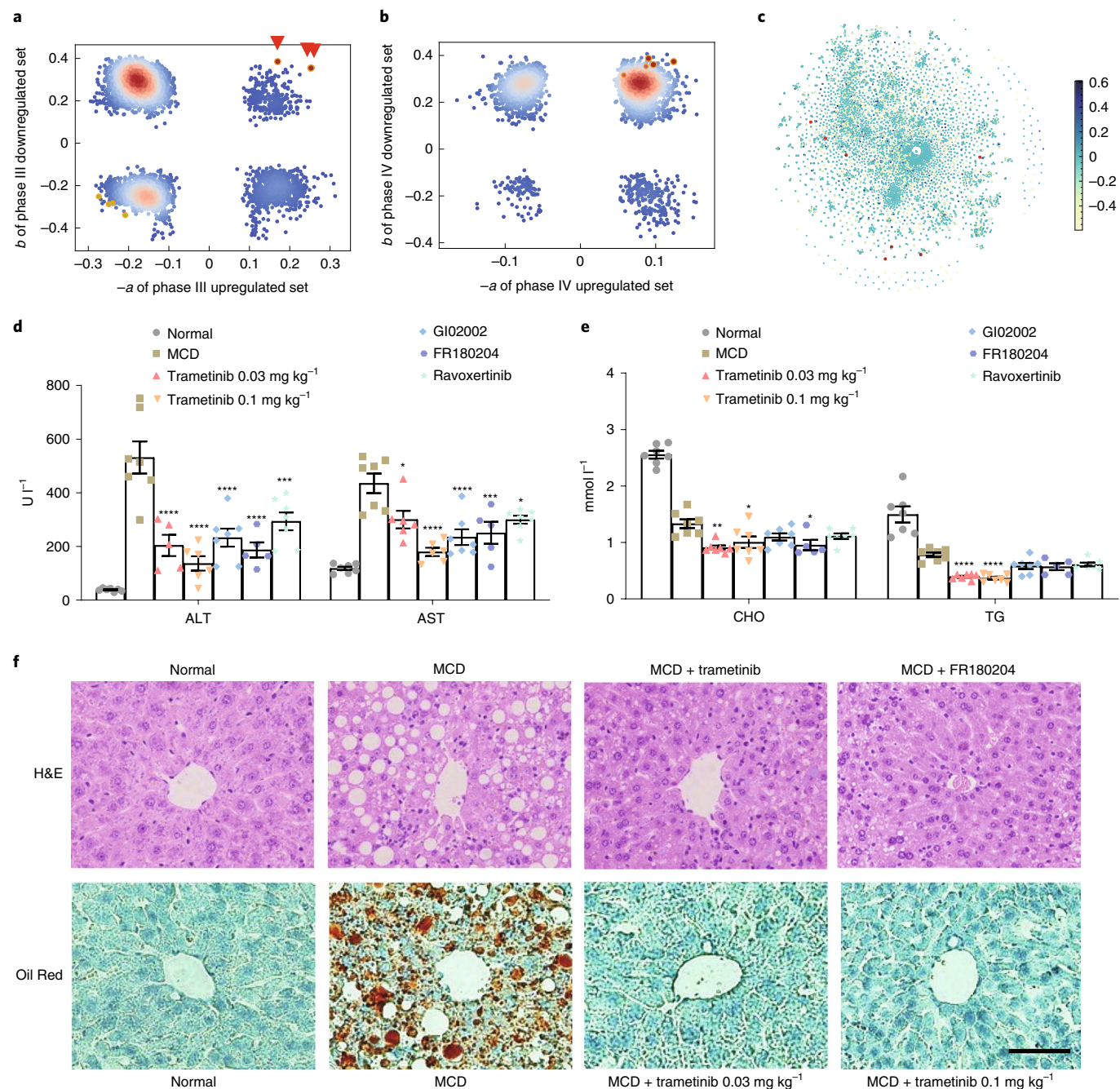


Fig. 5 | Trametinib and additional DLEPS-predicted compounds exert strong anti-NASH effects. **a**, A scatter plot of enrichment scores b versus $-a$ from DLEPS based on a clinical trial database library and using a set of previously published NASH stage III gene signatures as the genetic input. The red dots (two of which overlap) and arrows show the positive set while the yellow dots show the negative set. **b**, The same as in **a**, but with predictions made on the basis of NASH stage IV gene signatures and the D3680 library. **c**, t-SNE of the CDK fingerprints of the clinical trial database (input library); the highlighted dots in **a** are also highlighted here. **d-f**, 8-week-old mice were housed at 22°C, received normal or MCD diets for two weeks, and were then treated with trametinib (0.03 or 0.1 mg kg⁻¹), FR180204 (40 mg kg⁻¹) or vehicle (0.5% sodium carboxymethylcellulose containing 3% DMSO) by i.p. injection for 14 days. **d**, Serum ALT and AST levels ($n=7$ in the normal, MCD, GI02002 and ravoxertinib groups, $n=5$ in the trametinib (0.03 mg kg⁻¹) and FR180204 group, $n=6$ in the trametinib (0.1 mg kg⁻¹) group). **e**, Serum CHO and TG levels ($n=5$ in GI02002 group, and $n=7$ in the others). **f**, H&E and Oil Red staining of liver sections of MCD model mice (which exhibit many similarities to NASH symptoms in humans) that were treated with trametinib and FR180204 (3 mouse replicates). Scale bar, 100 μm. * $P < 0.05$, ** $P < 0.01$, *** $P < 0.001$, **** $P < 0.0001$ compared with the model group. All P values were determined by one-way analysis of variance. All data are presented as the mean \pm s.e.m.

lowered blood urea nitrogen (BUN; Fig. 4f), serum creatinine (Fig. 4g), alanine aminotransferase (ALT) and aspartate aminotransferase (AST) levels (Fig. 4h), decreased the kidney index (ratio of kidney and body weight; Extended Data Fig. 4b) and

reduced the degree of vacuolar fibrosis of renal tubules (Fig. 4i), consistent with DLEPS outputs.

To help elucidate perillen's mode of action in our HUA model mice, we tested whether perillen impacts xanthine oxidase (XOD), a

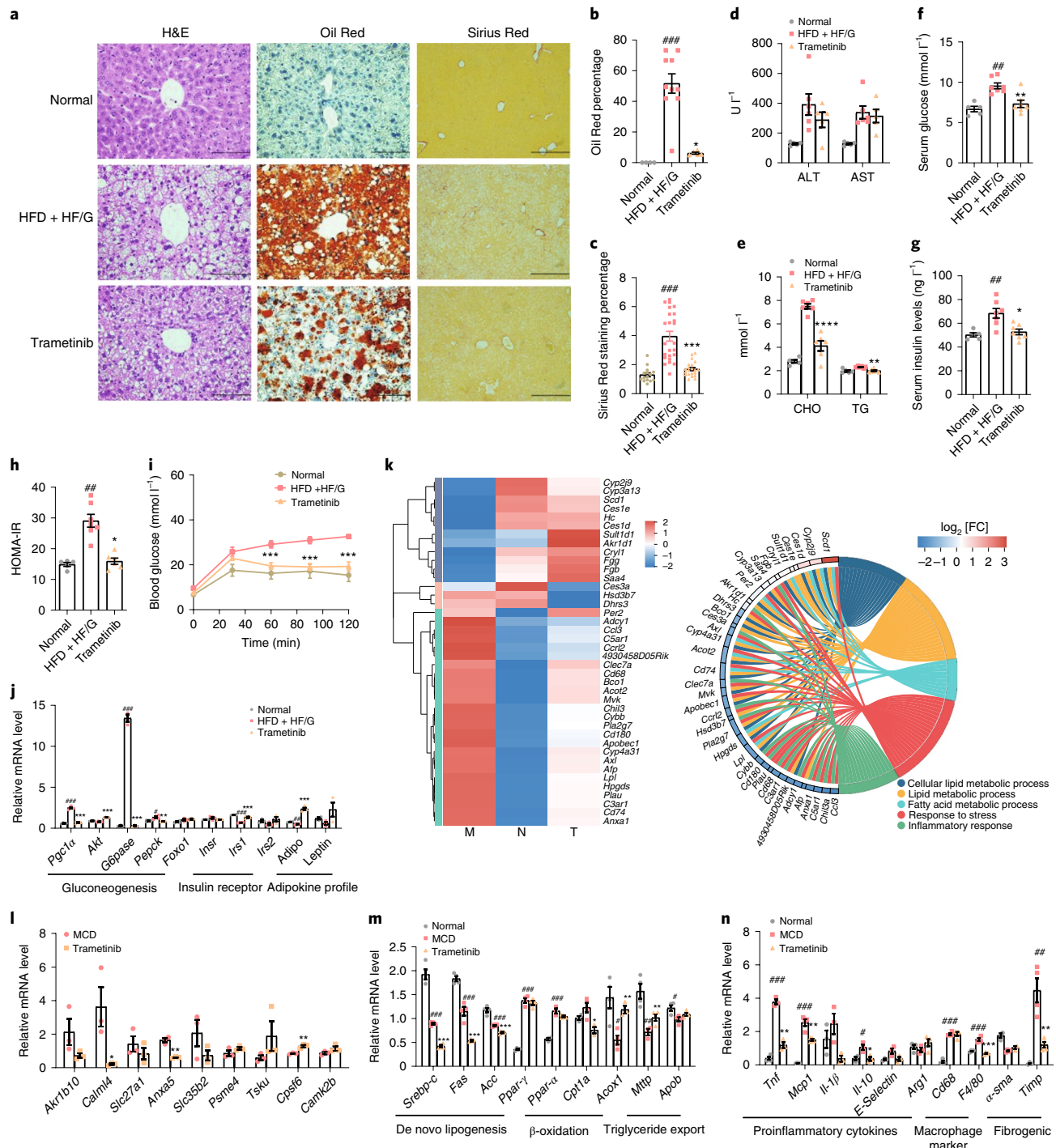


Fig. 6 | Trametinib rescues pathological changes in NASH. **a–j**, 8-week-old mice were housed at 22°C, received normal or HFD+HF/G diets for two weeks, and were then treated with trametinib (0.1 mg kg⁻¹) or vehicle (0.5% sodium carboxymethylcellulose containing 3% DMSO) by i.p. injection for 14 days. **a**, Left column: H&E staining of liver sections prepared from HFD+HF/G model mice. Scale bars, 100 μm. Middle column: Oil Red staining of HFD+HF/G model liver sections. Scale bars, 100 μm. Right column: Sirius Red staining of liver sections. Scale bars, 200 μm. **b–e**, Quantification of lipid content in liver (**b**), hepatic fibrosis in liver (**c**) (**b,c**, 3 mouse replicates), serum ALT and AST levels (**d**), and serum CHO and TG levels (**e**) (**d,e**, $n=5$ in the normal group, $n=6$ in the trametinib group, $n=7$ in the HFD+HF/G group). **f**, Fasting blood glucose in different groups ($n=5$ in the normal group, $n=7$ in the HFD+HF/G and trametinib groups). **g**, Serum insulin levels. **h**, HOMA-IR index. **i**, Plot of the i.p. glucose tolerance test (**g–i**, $n=5$ in the normal group, $n=7$ in the trametinib and HFD+HF/G groups). **j**, Quantitative PCR analysis of gluconeogenesis, insulin receptor and adipokine metabolism genes ($n=3$ for each group). **k–n**, 8-week-old mice were housed at 22°C, received normal or MCD diets for two weeks, and were then treated with trametinib or vehicle. **k**, Heatmap visualization and chord plot of GO terms related to inflammation and lipid metabolism. M, N and T represent MCD model, normal and trametinib-treated mouse groups, respectively. **l**, Quantitative PCR analysis of several genes that were part of the gene signatures used for DLEPS computation. **m**, Quantitative PCR analysis of the expression of genes from pathways including de novo lipogenesis, β-oxidation and TG export. **n**, Quantitative PCR analysis of the genes for proinflammatory cytokines as well as macrophage and fibrogenic markers (**k–n**, $n=3$ for each group).

* $P<0.05$, ** $P<0.01$, *** $P<0.001$, **** $P<0.0001$ compared with the model group. # $P<0.05$, ## $P<0.01$, ### $P<0.001$ compared with the normal group. All P values were determined by a two-tailed paired t-test. All data are presented as the mean \pm s.e.m.

known contributor to the pathogenesis of HUA^{24,25}. Indeed, perillen robustly decreased the activity of XOD in serum and in liver in the HUA model mice in a dose-dependent manner ($P < 0.01$, Fig. 4j,k). We further employed surface plasmon resonance (SPR) to determine whether perillen directly binds to XOD, and found that it does, with a dissociation constant (K_d) of 1.5 μM (Fig. 4l). See the Supplementary Information for transcriptional, extra DLEPS and pharmacokinetic analyses (Extended Data Fig. 4d–p) and enzyme-linked immunosorbent assay analysis of inflammation (Fig. 4m–o).

To sum up, deployment of DLEPS for HUA using two distinct types of gene signatures successfully identified multiple molecules that significantly reduce blood uric acid levels, inflammation and fibrosis in HUA model mice. Moreover, our mode-of-action studies revealed that perillen binds to and inhibits the activity of a known HUA-associated enzyme (XOD), an example of the potential clinical utility of hit molecules predicted by our system.

Identification of molecules against nonalcoholic steatohepatitis through iterative application of DLEPS. Having demonstrated the utility of our system for HUA, a relatively simple metabolic disorder with a well-understood etiology, we further extended the application of DLEPS to nonalcoholic steatohepatitis (NASH), a more complex disease without any well-established drug targets^{26–28}. NASH is understood as a contributor to the pathogenesis of liver cirrhosis and even liver cancer²⁸. Our study explored gene signatures from different NASH stages and included iterative use of successively narrower chemical libraries guided by our initial findings.

We first analyzed NASH gene signatures from a transcriptional analysis of visceral adipose tissue from obese patients diagnosed with NASH (stage III) and NASH with F2–F3 fibrosis (stage IV)²¹ (Supplementary Table 3). Note that we initially extended the input library to a clinical trial database including 11,294 compounds (Supplementary Table 2). The enrichment scores of up/downregulated genes (a/b , see Methods) are plotted as x and y coordinates in Fig. 5a (stage III, D11294 library) and Fig. 5b (stage IV, D3680 library). The top three positively scored molecules (brown dots in Fig. 5a,b) were chosen and visualized in the t-SNE space of CDK fingerprints (Fig. 5c). We again chose four of the negatively scored molecules (yellow dots in Fig. 5a) as a negative set.

Next, the NASH model was established by feeding mice a methionine- and choline-deficient (MCD) diet for 2 weeks; this resulted in hepatic steatosis, inflammation and increased ALT and AST levels (Fig. 5d–f). Treatment with trametinib and GI02002 markedly reduced the ALT, AST and triglyceride (TG) levels (Fig. 5d,e), rescued the pathological changes and reduced lipid accumulation (Fig. 5f and Extended Data Fig. 5a). Meanwhile, treatment with molecules in the negative set did not alleviate the ALT, AST, cholesterol (CHO), TG or steatosis phenotypes of the model mice (Extended Data Fig. 5b–d). Note that the NASH-related apoptosis of hepatocytes has been shown to cause hepatic stellate cell activation and leads to liver fibrosis²⁹. TdT-mediated dUTP nick end labeling revealed that model induction increased the number of apoptotic hepatocytes, and the trametinib treatment reduced the extent of hepatocyte apoptosis (Extended Data Fig. 5e).

We explored the effect of trametinib in greater detail in experiments using a HFD diet model induced with liquid fructose (HFD+HF/G), another common NASH model³⁰. Mice of this model are obese, insulin resistant and hyperglycemic, thus mirroring human NASH. Trametinib treatment eliminated lipid accumulation (Fig. 6a, second frame in bottom panel, and Fig. 6b), reduced the liver index (ratio of liver and body weight; Extended Data Fig. 6c) and substantially reduced the extent of collagen fiber staining (Fig. 6a, third frame in bottom panel, and Fig. 6c). Trametinib treatment also decreased the levels of ALT, AST, CHO and TG (Fig. 6d,e), and led to a remarkable reduction in serum glucose,

insulin and the homeostasis model assessment of insulin resistance (HOMA-IR) index³⁰ (Fig. 6f–h). Trametinib also reduced the glucose level in a glucose tolerance test (Fig. 6i).

Given that trametinib is known to be an efficient inhibitor of the MEK–ERK signaling pathway, and considering that previous studies have implicated the ERK1 or ERK2 proteins in glucose and lipid metabolism³¹, we hypothesized that other ERK inhibitors may exert effects similar to that of trametinib. We therefore explored a focused iteration of DLEPS using a refined library containing only 20 ERK inhibitors (Supplementary Table 2). We performed an experimental assessment of the top two hits from this library, raxoxertinib and FR180204, and found that these two molecules have similar effects to trametinib on ALT, AST, CHO and TG levels (Fig. 5d,e) and steatosis (Fig. 5f and Extended Data Fig. 5a). See the Supplementary Information for transcriptional analysis of trametinib-treated MCD model mice (related to Fig. 6k–n and Extended Data Fig. 6g).

To sum up, our exploration of DLEPS to identify anti-NASH drugs uncovered multiple hints that the ERK pathway should be investigated further as a vulnerable target for controlling NASH pathogenesis, and enabled our elaboration of DLEPS into a multi-step iterative pipeline based on the data-driven selection of refined libraries to pursue pathway-level etiopathological hypotheses.

Discussion

A major difficulty with target-protein-based drug discovery approaches is that the pathological mechanisms of many diseases remain unclear or involve many distinct pathways. To overcome this difficulty, we developed DLEPS, which supports prediction of candidate molecules for highly diverse and complex diseases with a requirement for only gene signatures. DLEPS examines and predicts CTPs. We trained DLEPS on the basis of more than one million transcriptional profiles associated with 17,051 structurally diverse small molecules that were generated by the L1000 project¹¹. Demonstrating DLEPS' capacity for generalization after its initial training, the Pearson correlation coefficient for CTP prediction for the test dataset was 0.74.

DLEPS takes chemical libraries and gene signatures of particular diseases as inputs. Here we demonstrated its use with FDA-approved drugs (961 molecules), natural molecules (2,719) and a clinical research compound database (11,294). In theory, our current implementation of DLEPS should work for any molecule that is shorter than 277 units in a grammar variational autoencoder (GVAE)¹³. Our study also extensively explored various gene signature inputs, including: a dual up/downregulated gene set from studies of obesity; for multiple phenotype manifestations in HUA; and for independent disease stage datasets (III/IV) in NASH. This capacity for extremely diverse disease-associated input datasets bears strong emphasis, as it suggests that our tool should be generally applicable for the identification of candidate disease treatment and research compounds for any of the tens of thousands of functional genomics studies conducted in recent decades, including microarrays and the current generation of RNA-sequencing (RNA-seq) technology.

Beyond its utility in identifying small molecules with biological activities relevant to disease or research contexts, DLEPS was also shown to yield insights into both pathogenic mechanisms and discovery of vulnerable target proteins and pathways. That is, our study with sequential, data-driven iterations revealed the importance of the ERK pathway in the pathogenesis of NASH. Our *in silico* tool highlights compounds for biologists to use when mutant-based studies have stalled or reached a dead end. Thus, the combination of DLEPS with diverse gene signatures can define a set of practical protocols for researchers. Experiments designed for both hit development and target discovery will often go well beyond the scope of many initially mutant-based studies.

Online content

Any methods, additional references, Nature Research reporting summaries, source data, extended data, supplementary information, acknowledgements, peer review information; details of author contributions and competing interests; and statements of data and code availability are available at <https://doi.org/10.1038/s41587-021-00946-z>.

Received: 8 October 2020; Accepted: 6 May 2021;

Published online: 17 June 2021

References

- Kong, W. et al. Prediction and optimization of NaV1.7 sodium channel inhibitors based on machine learning and simulated annealing. *J. Chem. Inf. Model.* **60**, 2739–2753 (2020).
- Lyu, J. et al. Ultra-large library docking for discovering new chemotypes. *Nature* **566**, 224–229 (2019).
- Segler, M. H. S., Preuss, M. & Waller, M. P. Planning chemical syntheses with deep neural networks and symbolic AI. *Nature* **555**, 604–610 (2018).
- Xu, Y. et al. Deep learning for drug-induced liver injury. *J. Chem. Inf. Model.* **55**, 2085–2093 (2015).
- Zhavoronkov, A. et al. Deep learning enables rapid identification of potent DDR1 kinase inhibitors. *Nat. Biotechnol.* **37**, 1038–1040 (2019).
- Stokes, J. M. et al. A deep learning approach to antibiotic discovery. *Cell* **180**, 688–702 (2020).
- Lamb, J. et al. The Connectivity Map: using gene-expression signatures to connect small molecules, genes, and disease. *Science* **313**, 1929–1935 (2006).
- Lee, J. et al. Withaferin A is a leptin sensitizer with strong antidiabetic properties in mice. *Nat. Med.* **22**, 1023–1032 (2016).
- Liu, J., Lee, J., Salazar Hernandez, M. A., Mazitschek, R. & Ozcan, U. Treatment of obesity with celastrol. *Cell* **161**, 999–1011 (2015).
- Wang, Y. et al. Multiple-purpose connectivity map analysis reveals the benefits of esculetin to hyperuricemia and renal fibrosis. *Int. J. Mol. Sci.* **21**, 7695 (2020).
- Subramanian, A. et al. A next generation connectivity map: L1000 platform and the first 1,000,000 profiles. *Cell* **171**, 1437–1452 (2017).
- Subramanian, A. et al. Gene set enrichment analysis: a knowledge-based approach for interpreting genome-wide expression profiles. *Proc. Natl Acad. Sci. USA* **102**, 15545–15550 (2005).
- Kusner, M. et al. Grammar variational autoencoder. *Proc. 34th Int. Conf. Machine Learning, PMLR* **70**, 1945–1954 (2017).
- Galmozzi, A. et al. ThermoMouse: an *in vivo* model to identify modulators of UCP1 expression in brown adipose tissue. *Cell Rep.* **9**, 1584–1593 (2014).
- Seale, P. et al. Transcriptional control of brown fat determination by PRDM16. *Cell Metab.* **6**, 38–54 (2007).
- Jalal, D. I., Chonchol, M., Chen, W. & Targher, G. Uric acid as a target of therapy in CKD. *Am. J. Kidney Dis.* **61**, 134–146 (2013).
- Puddu, P., Puddu, G. M., Cravero, E., Vizioli, L. & Muscari, A. Relationships among hyperuricemia, endothelial dysfunction and cardiovascular disease: molecular mechanisms and clinical implications. *J. Cardiol.* **59**, 235–242 (2012).
- Toda, A., Ishizaka, Y., Tani, M. & Yamakado, M. Hyperuricemia is a significant risk factor for the onset of chronic kidney disease. *Nephron Clin. Pract.* **126**, 33–38 (2014).
- Verhaeghe, C. et al. Role of IKK and ERK pathways in intrinsic inflammation of cystic fibrosis airways. *Biochem. Pharmacol.* **73**, 1982–1994 (2007).
- Ramnath, D. et al. Hepatic expression profiling identifies steatosis-independent and steatosis-driven advanced fibrosis genes. *JCI Insight* **3**, e120274 (2018).
- du Plessis, J. et al. Association of adipose tissue inflammation with histologic severity of nonalcoholic fatty liver disease. *Gastroenterology* **149**, 635–648 (2015).
- Chang, H. H., Chen, C. S. & Lin, J. Y. Dietary perilla oil inhibits proinflammatory cytokine production in the bronchoalveolar lavage fluid of ovalbumin-challenged mice. *Lipids* **43**, 499–506 (2008).
- Chen, T. et al. Perilla oil supplementation ameliorates high-fat/high-cholesterol diet induced nonalcoholic fatty liver disease in rats via enhanced fecal cholesterol and bile acid excretion. *Biomed Res. Int.* **2016**, 2384561 (2016).
- Ernst, M. E. & Fravel, M. A. Febuxostat: a selective xanthine-oxidase/xanthine-dehydrogenase inhibitor for the management of hyperuricemia in adults with gout. *Clin. Ther.* **31**, 2503–2518 (2009).
- Krakoff, I. H. & Meyer, R. L. Prevention of hyperuricemia in leukemia and lymphoma: use of allopurinol, a xanthine oxidase inhibitor. *JAMA* **193**, 1–6 (1965).
- Banini, B. A. & Sanyal, A. J. Current and future pharmacologic treatment of nonalcoholic steatohepatitis. *Curr. Opin. Gastroenterol.* **33**, 134–141 (2017).
- Sumida, Y. & Yoneda, M. Current and future pharmacological therapies for NAFLD/NASH. *J. Gastroenterol.* **53**, 362–376 (2018).
- Anstee, Q. M., Reeves, H. L., Kotsilitsi, E., Govaere, O. & Heikenwalder, M. From NASH to HCC: current concepts and future challenges. *Nat. Rev. Gastroenterol. Hepatol.* **16**, 411–428 (2019).
- Eguchi, A., De Mollerat Du Jeu, X., Johnson, C. D., Nektaria, A. & Feldstein, A. E. Liver Bid suppression for treatment of fibrosis associated with non-alcoholic steatohepatitis. *J. Hepatol.* **64**, 699–707 (2016).
- Liu, X. J. et al. Characterization of a murine nonalcoholic steatohepatitis model induced by high fat high calorie diet plus fructose and glucose in drinking water. *Lab. Invest.* **98**, 1184–1199 (2018).
- Lawan, A. & Bennett, A. M. Mitogen-activated protein kinase regulation in hepatic metabolism. *Trends Endocrinol. Metab.* **28**, 868–878 (2017).

Publisher's note Springer Nature remains neutral with regard to jurisdictional claims in published maps and institutional affiliations.

© The Author(s), under exclusive licence to Springer Nature America, Inc. 2021

Methods

Data processing. The L1000 data were obtained from the Library of Integrated Network-Based Cellular Signatures project¹¹. The data were downloaded from <https://www.ncbi.nlm.nih.gov/geo/query/acc.cgi?acc=GSE92742>. The SHA512 code was tested to ensure the integrity of the data. Then we performed data cleaning using the following criteria: the molecules must have more than five replicates; the molecule SMILE should be successfully parsed using rdkit (version 2017.9.01). We averaged all of the profiles for each molecule by ignoring plate, dose, treatment time and cell line details. We fitted only the landmark genes. Finally, we obtained 17,051 valid molecules, and these data were split into training (14,051), validation (1,500) and test (1,500) sets.

Encoding SMILES into latent vectors and training the deep neural network.

We tried different ways to encode SMILES of chemical compounds into latent vectors. SMILES can be encoded into latent space as plain text through a variational autoencoder. In another way, SMILES can be initially converted to a grammar tree (GVAE)¹³. We found that both ways worked well. Finally, we used GVAE as the encoding model. The molecules were first represented by canonical SMILES processed by rdkit, then parsed to a grammar tree (76 node types), and then to a flattened vector, which was then converted to a one-hot array (maximum length 277, data dimension (277, 76), which was then passed to three layers of one-dimensional convolutional neural networks (Conv1D(9, 9) with output dimension (269, 9), Conv1D(9, 9) with output dimension (261, 9), Conv1D(10, 11) with output dimension (251, 10)). The output slices were flattened (dim = 2,510) and then passed to a dense layer, which output the mean vector (dim = 56) and radius vector (dim = 56) to encode a sphere in high-dimensional space¹³. The coordinates of a randomly sampled dot (dim = 56) in this sphere were chosen as the latent vector, which was then passed through a five-layer dense network (output dim = 1,024; each followed a dropout layer with dropout rate = 0.25; the activation function of the first three layers is relu, that of the fourth layer is tanh, that of the fifth layer is linear) for prediction of change of transcriptional profiles (CTPs, 978 landmark genes). Finally, 978 landmark genes were converted to 12,328 genes through linear transformation. The dropout layers were adopted to overcome overfitting. The role of the tanh function is to make the output in the range of [-1, 1]. The linear layer after that is to output in the range [-∞, +∞]. Note that this setup is essential for good fitting. The conversion matrix from 978 landmark genes to 12,328 genes was obtained from the L1000 project. We used a pretrained GVAE model with fixed parameters for the first-step training (30,000 steps). Then all of the parameters were fine-tuned for another 10,000 steps. We used mean squared error as our cost function, and Adam as our optimizer algorithm. We evaluated the performance of our network with the Pearson correlation coefficient. We defined a ROC-like curve by setting a threshold Pearson r and plotted fraction($r > r_{\text{threshold}}$). Thus, the AUC is actually the mean Pearson r because x spans a unit distance. This ROC-like curve provided a better understanding of the fitting for those who are familiar with ROC.

Analysis of DLEPS' performance. From the combined validation and test sets (V/T set), 2,033 (68%) molecules were well predicted ($r > 0.74$). First, a pair of molecules from the V/T set and the training set with Tanimoto similarity > 0.35 based on the CDK fingerprints were identified. A CDK fingerprint contains 1,024 bits. The Tanimoto similarity is defined as:

$$\text{TS} = \frac{c}{a + b - c}$$

where a is the number of ones in the first molecule, b is the number of ones in the second molecule and c is the number of ones shared between the two molecules.

For any pair of molecules, we first calculated the maximum common sub-structures by rdkit. Then, we obtained the differential fragments by subtracting the maximum common sub-structures. The fragment descriptors of these differential fragments were calculated by the MoleculeDescriptors package, which includes 85 fragment descriptors, in rdkit. The Wilcoxon rank-sum test, which is an exact measure of probability (nonparametric test), was employed to characterize the statistical difference of fragments' occurrence in well-correlated and uncorrelated molecule pairs.

Computation of enrichment score. The Kolmogorov-Smirnov test was used to evaluate the distribution of the query genes in the reference list. The CTPs were calculated by DLEPS and used to make the rank list (12,328 genes). The enrichment score for the upregulated gene set is defined as

$$a = \max_{j=1 \text{ to } t} \left[\frac{j}{t} - \frac{V(j)}{n} \right]$$

where t is the number of genes in the query gene set, n is the number of genes in the computed CTPs, and $V(j)$ is the rank of a specific gene in the rank list. The enrichment score for the downregulated gene set is defined as

$$b = - \max_{j=1 \text{ to } t} \left[\frac{V(j) - 1}{n} - \frac{j - 1}{t} \right]$$

The score is defined as¹²

$$\text{Score} = \begin{cases} a - b & \text{when } b \times a < 0 \\ 0 & \text{when } b \times a > 0 \end{cases}$$

Note that $(-1) \times [a, b]$ or $(b - a)$ means to reverse the gene signatures. As shown in Figs. 4a and 5a,b, we plotted b versus $-a$; thus, the upper right corner shows positively predicted molecules. In Figs. 3a and 4b, we plotted the first $(b - a)$ versus the second $(b - a)$; again, the upper right corner shows positively predicted molecules.

Small-molecule libraries. In this research, a natural compound library (L6000, TargetMol, $n = 2,719$) and an FDA-approved library (L4200, TargetMol, $n = 961$), merged as D3680, were used to screen the positive chemicals in obesity and HUA. D3680 was also used with the NASH stage IV markers. Clinical trial molecules (11,294) from DrugBank were used with the NASH stage III markers (<https://www.drugbank.ca/releases/latest>). DLEPS works for all kinds of small molecules with grammar encoding length < 277 .

Identification of gene signatures. In HUA, the inflammation/fibrosis gene signatures were generated by comparison of fetal tracheal cells (CFT2, carrying the homozygous deletion ΔF508) and NT-1 cells¹⁹. Microarray analysis identified the genes involved in inflammation, fibrosis and matrix remodeling. The upregulated genes included those encoding adhesion molecules (ICAM1, ITGA2, ITGA3, ITGA4, ITGA6, CD44, KITLG and COL13A1), chemokines and cytokines (IL1B, IL6 and IL-8), and products involved in the NF-κB-AP-1 pathway (PTGS2, TNFRSF21, TNFRSF11A, TNFRSF10A, TNFRSF19, TNFAIP6, TNFAIP63, A20, IKBIA and IRAK2) and matrix remodeling (MMP1, MMP2, MMP3, MMP14, PLA2U, PLAUR and ADAMTS3). The downregulated genes included those encoding adhesion molecules (ITGA11, ITGA7, COL5A3, COL11A1, COL15A1, COL4A1, COL8A1 and COL4A2), cytokine receptors (IL6R, PDGFRA, PDGFRB, IL1RAP, INHBE, CCR5 and FLT1), and products involved in the NF-κB-AP-1 pathway (TRAF5 and TLR4) and matrix remodeling (MMP16, ADAM33, ADAMTS2 and ADAMTS5). To confirm the efficacy of the aforementioned inflammation/fibrosis score, we adopted DEGs of RNA-seq of liver from patients with hepatitis C virus ($n = 55$, with (26) or without (29) steatosis) or fatty liver ($n = 14$, with 12 nonalcoholic fatty liver disease and 2 alcohol-related fatty liver disease) for extra analysis. The patient cohort has been subdivided into early and advanced fibrosis²⁰. The top 50 upregulated genes and top 44 downregulated genes were used to calculate the hepatic steatosis scores. In NASH, the up/downregulated gene sets were obtained from RNA-seq of tissues from obese patients ($n = 113$ subjected to four groups: obese, NAFL, NASH and NASH with fibrosis). A fold threshold was used for the cutoff. In obesity, the upregulated genes and downregulated genes were obtained from RNA-seq of mouse adipose tissues, and then we converted the mouse gene identifiers into human gene identifiers. After inputting the list of upregulated and downregulated genes, we got a rank score of these chemicals, in which the top molecules were chosen. Then we looked for literature to decide the final molecules for the experiment on the basis of the following conditions: there was no literature or patents reporting the molecule to be effective against the disease we aimed to target; it was better to have an effective concentration already reported in other functional studies; it was better to be safe for use in animals or humans.

Other computational tools. CDK fingerprints were calculated by the rcdk package in R. Morgan fingerprints and Tanimoto similarities were calculated by rdkit in Python. To fully reproduce DLEPS prediction in obesity, rdkit 2017.09.1 was required to obtain the canonical SMILES. For HUA, a 'setmean' option, meaning subtracting the mean CTPs of the D3680 library rather than the mean CTPs from the L1000 data, has been enabled for CTP calculation. t-SNE and k-means clustering were performed by the scikit-learn package in Python. The deep learning model was constructed by keras (2.3.0) using the TensorFlow (1.5.0) backend. Figures related to computation were plotted by matplotlib in Python. Experimental figures were plotted by GraphPad Prism 6.01.

Obesity and WAT browning. Mice. The animal experiments in this section and the following two sections were performed in strict accordance with the guidelines of the Ethics Committee of Peking University Health Science Center (LA2016113 and LA2018189) and approved by the Animal Care and Use Committee of Peking University. C57BL/6 male mice were obtained from the Department of Laboratory Animal Science of Peking University Health Science Center and the Beijing branch of Charles River Laboratories (Beijing Vital River Laboratory Animal Technology Co.). Mice were housed under controlled light (12-h dark-light cycle, with the dark cycle encompassing 20:00 to 8:00), temperature ($22 \pm 2^\circ\text{C}$) and humidity ($50 \pm 10\%$) conditions with a free access to food and water. For diet-induced obesity studies, mice were placed on a diet containing 60 kcal% fat (HFD; Research Diets, D12492) at the age of 8 weeks. During all procedures of the experiments, the number of animals and their suffering by treatments were minimized.

Reagents. UCP1-, PGC1α- and β-actin-specific antibodies were purchased from Abcam (ab-10983), Santa Cruz Biotechnologies (sc-13067) and Sigma (A5316).

Tranzol Up, TransScript One-step gDNA Removal and cDNA Synthesis Super MiX, and TransStart Top Green quantitative PCR Super Mix were purchased from TransGen Biotech. RNaseZap was purchased from Invitrogen. The enhanced chemiluminescence assay kit was purchased from Bio-Rad. Isoginkgetin (CAS 548-19-6, catalog no. T4S21320), loureirin B (CAS 119425-90-0, catalog no. T3876) and chikusetsusaponin IV (CAS 7518-22-1, catalog no. T4S0290) were purchased from TargetMol. Mudanpioside C (CAS 172760-03-1, catalog no. DM0065), agnuside (CAS 11027-63-7, catalog no. DH0098), syringic acid (CAS 530-57-4, catalog no. DL0057) and 13-acetyl-9-dihydrobaccatin-III (CAS 142203-65-4, catalog no. DY0457) were purchased from Chengdu DeSiTe Biological Technology Co. DMSO was purchased from Amresco.

Administration of I/L/C. For i.p. treatment, mice received 25 µl of vehicle (DMSO) for 4 days as acclimation. Then, I/L/C were dissolved in DMSO (25 µl) respectively, and administered to mice once a day for 14 days (isoginkgetin, 3 mg kg⁻¹; loureirin B, 1 mg kg⁻¹; chikusetsusaponin IV, 20 mg kg⁻¹). Vehicle groups received 25 µl of DMSO during the course of the experiments. All treatments were performed within 90 min before the dark cycle. We determined the dosages of the three compounds on the basis of the published literature^{32–36} and our own experiments.

Food intake and body weight measurements. Food intake and body weight were measured daily, and the percentage increase of body weight was calculated by the following equation: 100 × (body weight – initial body weight)/(initial body weight).

Magnetic resonance imaging measurements. Subjects were imaged by a magnetic resonance imaging scanner (EchoMRI-700) using a prospectively designed and validated method of fat mass prediction from a single magnetic resonance imaging slice at the L2–L3 intervertebral level. Fat volumes were converted to mass using 0.9196 kg l⁻¹ as the density of TG in adipose tissue.

H&E staining. iWATs were collected from mice treated with isoginkgetin (3 mg kg⁻¹), loureirin B (1 mg kg⁻¹), chikusetsusaponin IV (20 mg kg⁻¹) or DMSO for 2 weeks, and immediately fixed in 4% paraformaldehyde solution for 48 h. Then the samples were embedded in optimal cutting temperature OCT compound (Sakura FineTech). Tissue sections of 10 µm thickness were stained with H&E. Stained slides were analyzed using an indicated magnification, and images were captured by a digital camera (Olympus).

Quantitative real-time PCR. Total RNA for quantitative real-time PCR was extracted from fat pads using TRIzol reagent (TransGen Biotech) by following the manufacturer's protocol. Quantification and integrity analysis of total RNA was performed by running 1 µl of each sample on a NanoDrop 5500 (Thermo). cDNA was prepared by reverse transcription (TransScript one-step gDNA removal and cDNA synthesis Super MiX, TransGen Biotech). The relative expression of mRNAs was determined by the SYBR Green PCR system (Bio-Rad). The relative expression of the genes of interest was calculated by the comparative Ct method and GAPDH was used as an endogenous control. The sequences of the primers used for real-time quantitative PCR are available in Supplementary Table 5.

Total protein extraction and western analysis. iWATs were homogenized with a Polytron in ice-cold RIPA buffer supplemented with protease and phosphatase inhibitors (catalog no. P8340 and no. P2850; Sigma). Protein concentration in the supernatant was determined by a bicinchoninic acid assay (Aidlab; PP01). Band intensities were quantified using ImageJ software (NIH).

Indirect calorimetry. After adaptation to single caging, mice were placed in metabolic chambers on day 13 of I/L/C or DMSO treatment, respectively. After a 24 h acclimation, we administered isoginkgetin (3 mg kg⁻¹), loureirin B (1 mg kg⁻¹), chikusetsusaponin IV (20 mg kg⁻¹) or DMSO within 90 min before the dark cycle.

Indirect calorimetry recording was performed using an indirect open-circuit calorimeter Oxylet Physiocal System (LE1305 Physiocal 00; LE405 O₂/CO₂ Analyzer; LE400 Air Supply and Switching; Panlab).

The \dot{V}_{O_2} and \dot{V}_{CO_2} values are expressed in milliliters per minute per kilogram. The RER was determined by the ratio $\dot{V}_{CO_2}/\dot{V}_{O_2}$. The EE was calculated according to the following equation: EE (kcal d⁻¹ kg⁻¹) = $\dot{V}_{O_2} \times 1.44 \times [3.815 + (1.232 \times RER)]$. The mean values for \dot{V}_{O_2} , \dot{V}_{CO_2} , RER and EE of the dark cycle and the light cycle were compared for each group.

HUA. Materials. Perillen (CAS 539-52-6, catalog no. DZ0047) was purchased from Chengdu DeSiTe Biological Technology Co. Allopurinol (CAS 315-30-0, catalog no. A0907), topiroxostat (CAS 577778-58-6, catalog no. T21294), febuxostat (CAS 144060-53-7, catalog no. F31133), benzboromarone (CAS 3562-84-3, catalog no. M026978), hypoxanthine (CAS 68-94-0, catalog no. M056842) and potassium oxonate (CAS 2207-75-2, catalog no. M026814) were purchased from Meridian Medical Technologies. The BUN assay kit, uric acid test kit, creatinine assay kit (sarcosine oxidase type), ALT assay kit, AST assay kit, serum XOD assay kit, TNF assay kit, IL-1 β assay kit and IL-6 assay kit were all purchased from Nanjing Jiancheng Bioengineering Institute.

HUA therapeutic animal model. To explore the anti-HUA activity of perillen, HUA was induced by hypoxanthine and potassium oxonate, as a uricase inhibitor and substrate of XOD. The mice were randomly divided into the necessary groups, with six animals in each group. The control mice received 0.9% saline solution as a vehicle. In hyperuricemic mice, a mixture of hypoxanthine and potassium oxonate (300 mg kg⁻¹) was injected intraperitoneally. In the treatment groups, perillen, allopurinol, topiroxostat, febuxostat or benzboromarone (as positive control) was orally administrated 3 h after hypoxanthine and potassium oxonate injection and then once daily for 3, 7 and 14 days.

Measurement of physiological parameters and XOD activities. Serum uric acid was assayed using a uric acid test kit. BUN was assayed using a urea nitrogen assay kit. Creatinine was assayed using a creatinine assay kit. ALT was assayed using an ALT assay kit. AST was assayed using an AST assay kit. Serum XOD activity was assayed using an XOD assay kit and serum TNF/IL-6/IL-1 β was assayed using a TNF/IL-6/IL-1 β assay kit. For determination of XOD activity in liver, 0.5 g of liver was homogenized on ice in 2.5 ml phosphate buffer (50 mM, pH 7.4). The homogenates were centrifuged at 3,000g for 10 min at 4 °C, and the supernatants were then carefully removed and subjected to further centrifugation at 15,000g for 60 min at 4 °C. The supernatants were then used for further analyses.

SPR biosensor analysis. The binding affinity of perillen to XOD in vitro was assayed using the SPR-based Biacore 3000 instrument (Biacore AB). XOD protein was purchased from Sigma-Aldrich. The method was described by Si et al.³⁷

Serum concentration of perillen analysis. A gas chromatography–mass spectrometry (GC–MS) method was modified from that described by Cetin et al.³⁸ and validated to determine the concentration of perillen in mouse plasma. Plasma samples (50 µl) were mixed with 150 µl of internal standard (cineol, dissolved in hexane) for liquid–liquid extraction. The mixture was vortexed for approximately 5 min, and then centrifuged at 15,000 r.p.m. for 8 min. The supernatant (100 µl) was injected into the GC system for analysis. A Thermo Trace GC Ultra/DSQII equipped with a Triplus auto sampler, an Agilent DB-624 capillary column (30 m × 0.32 mm, 0.5 µm) and an electrospray ionization source was used for MS analysis. The basic parameters for GC–MS systems were in accordance with those described by Cetin et al. Briefly, helium served as the carrier gas with a constant flow rate of 2 ml min⁻¹. The gas flow was split 5:1 into the MS detector. Both the injection temperature and source temperature were set at 250 °C. The data were acquired in selected ion monitoring mode and processed using the Xcalibur software (Thermo, version 2.2). The mass-to-charge ratio (*m/z*) for the internal standard and perillen was 154 and 150, respectively. Calibration of perillen in plasma was linear (*r*² ≥ 0.999) in the range of 5 to 5000 ng ml⁻¹. The accuracy of the method ranged from 85.4% to 114.96%. All samples analyzed complied with the acceptance criteria for standard curve and quality control samples.

A preliminary pharmacokinetics study of perillen. Twelve male KM mice, 8–10 weeks old, weighing 27 ± 3 g were obtained from SPF (Beijing) Biotechnology Co., Ltd. Environmental controls for the animal room were set at 22 ± 3 °C with 50 ± 20% relative humidity. The animal studies were carried out in accordance with the requirements of Chinese national legislation. After overnight fasting but with free access to drinking water, these mice were administered a single dose of perillen solution (3, 10, 30 mg kg⁻¹ by gavage and 3 mg kg⁻¹ by tail vein injection, respectively). Blood samples (0.2 ml) were drawn from the ophthalmic venous plexus at predose and 0.25, 0.5, 0.75, 1, 1.5, 2, 4, 6 and 8 h post-dosing in K2EDTA anticoagulant tubes. The blood samples for each time point were collected from one mouse. Each blood sample was centrifuged at 8,000 r.p.m. for 5 min and the plasma was stored at –80 °C until analysis.

NASH. Reagents. Trametinib (CAS 871700-17-3, catalog no. T2125), raxovertinib (CAS 1453848-26-4, catalog no. T6511), FR180204 (CAS 865362-74-9, catalog no. T195), nomilin (CAS 1063-77-0, catalog no. T3672), luponone (CAS 1617-70-5, catalog no. T5708), bendroflumethiazide (CAS 73-48-3, catalog no. T1204), butoconazole (CAS 64872-76-0, catalog no. T8490), benfotiamine (CAS 22457-89-2, catalog no. T1129), menaquinone-4 (CAS863-61-6, catalog no. T7106) and phenacetin (CAS 62-44-2, catalog no. T0778) were purchased from TargetMol. Telmisartan (CAS 144701-48-4) and GI02002 were purchased from Chengdu DeSiTe Biological Technology Co.

Animal experiments. C57BL/6 male mice were obtained from the Department of Laboratory Animal Science of Peking University Health Science Center. Where indicated, 8-week-old male mice were assigned to receive normal chow diet or MCD diet for 4 weeks or HFD + HF/G (catalog no. D12492, Research Diet; 23.1 g L-fructose plus 18.9 g L-glucose in 11 of tap water, catalog nos. F3510 and G8270, Sigma-Aldrich) for 16 weeks (HFD for weeks 1–16 and HF/G for weeks 9–16). Mice were treated with vehicle (0.5% sodium carboxymethylcellulose) or trametinib (0.03 mg kg⁻¹ or 0.1 mg kg⁻¹) by i.p. injection after two weeks' MCD diet or 16 weeks' HFD + HF/G diet for 14 d. Mice were anesthetized with isoflurane and killed, and the liver tissues and blood samples were collected for evaluation. Plasma was obtained by centrifugation of the blood at 2,000g for 10 min.

Biochemical analysis and histopathology. ALT, AST, serum TG and CHO were assessed by an automatic biochemical analyzer. The serum insulin level was measured with a mouse insulin enzyme-linked immunosorbent assay kit (F10124-B). The HOMA-IR index was calculated following the formula: HOMA-IR = (fasting serum insulin ($\mu\text{U l}^{-1}$) \times fasting serum glucose (mmol l^{-1})) / 22.5. Liver tissue in 4% paraformaldehyde was stained with H&E to observe the damage and was subjected to Oil Red staining to visualize lipid droplets in the liver. Liver fibrosis was observed by Sirius Red staining. The images were captured and analyzed using a microscope (NI, Nikon). The results of the Oil Red analysis were quantified according to the method in a previous study³⁰. The results of the Sirius Red staining were quantified using ImageJ software.

Quantitative real-time PCR. Target mRNA levels were adjusted relative to the values for GAPDH, which was used as the endogenous control. The primers used to detect the genes are listed in Supplementary Table 5.

Intraperitoneal glucose tolerance test. Mice were injected intraperitoneally with glucose (2 g kg^{-1} body weight) after being fasted for 12 h. The glucose level was measured at 0, 30, 60, 90 and 120 min after injection by a glucometer (catalog no. RC-6454011-50; Active Blood Glucose Meter).

Determination of doses. We determined the dosages of three compounds (trametinib (0.03 and 0.1 mg kg^{-1}), raxovertinib (1 mg kg^{-1}) and FR180204 (40 mg kg^{-1})) on the basis of the published literature^{40–45}. These studies mainly highlight the anticancer and antiarthritis effects of these agents. Notably, the doses of these compounds used in the studies here showed significant tumor suppressive and antiarthritis effects, providing an appropriate dosage range for each compound.

Analysis of transcriptions. The DEGs between normal and NASH liver tissues were also screened by the limma package. $|\log_2[\text{FC}]| \geq 1$, P value < 0.05 were considered statistically significant for the DEGs. To elucidate potential biological processes, molecular functions and cellular components associated with the DEGs, we performed Gene Ontology (GO) enrichment analysis utilizing the Database for Annotation, Visualization and Integrated Discovery, and Kyoto Encyclopedia of Genes and Genomes pathway enrichment analysis was carried out by clusterProfiler to expound promising signaling pathways correlated with the DEGs. A P value < 0.05 was defined as the cutoff criterion.

Reporting Summary. Further information on research design is available in the Nature Research Reporting Summary linked to this article.

Data availability

The training and test data for DLEPS were downloaded from the Gene Expression Omnibus with the accession number [GSE92742](#). Browning markers, inflammation and fibrosis markers, and NASH markers were analyzed from ArrayExpress with accession numbers [E-GEOD-8044](#), [E-MEXP-980](#), [E-GEOD-58979](#), respectively. All gene signatures are listed in Supplementary Table 3. RNA-seq data for WAT from mice treated with chikusetsusaponin IV and control mice ([GSE165171](#)), kidney from perillen-treated and control mice ([GSE165173](#)) and liver from trametinib-treated and control mice ([GSE165174](#)) are available at the Gene Expression Omnibus. Source data are provided with this paper.

Code availability

The code for DLEPS is available at <https://github.com/kekegg/DLEPS>. We have also set up a user-friendly online computing interface (<https://www.dleps.tech/dleps/index>). Commercial use of DLEPS requires a license.

References

32. Jiang, Y. et al. Bioactivity-guided fractionation of the traditional Chinese medicine Resina Draconis reveals loureirin B as a PAI-1 inhibitor. *Evid. Based Complement. Alternat. Med.* **2017**, 9425963 (2017).
33. Liu, Y. H. et al. Loureirin B suppresses RANKL-induced osteoclastogenesis and ovariectomized osteoporosis via attenuating NFATc1 and ROS activities. *Theranostics* **9**, 4648–4662 (2019).
34. Xin, Y., Yuan, Q., Liu, C., Zhang, C. & Yuan, D. MiR-155/GSK-3β mediates anti-inflammatory effect of Chikusetsusaponin IVa by inhibiting NF-κB signaling pathway in LPS-induced RAW264.7 cell. *Sci. Rep.* **10**, 18303 (2020).
35. Zhao, C. M., Han, S., Yang, S. B. & Xin, W. D. Validation and application of a novel LC/MS/MS method for the determination of isoginkgetin in rat plasma. *Biomed. Chromatogr.* **33**, e4667 (2019).
36. Shi, Y. R. et al. Imaging of pre-mRNA splicing in living subjects using a genetically encoded luciferase reporter. *Biomed. Opt. Express* **9**, 518–528 (2018).
37. Si, L. et al. Triterpenoids manipulate a broad range of virus-host fusion via wrapping the HR2 domain prevalent in viral envelopes. *Sci. Adv.* **4**, eaau8408 (2018).
38. Cetin, B. et al. Antimicrobial activities of essential oil and hexane extract of Florence fennel [*Foeniculum vulgare* var. *azoricum* (Mill.) Thell.] against foodborne microorganisms. *J. Med. Food* **13**, 196–204 (2010).
39. Zhong, D. D. et al. *Ganoderma lucidum* polysaccharide peptide alleviates hepatotaxis via modulating bile acid metabolism dependent on FXR-SHP/FGF. *Cell. Physiol. Biochem.* **49**, 1204–1220 (2018).
40. Yamaguchi, T., Kakefuda, R., Tajima, N., Sowa, Y. & Sakai, T. Antitumor activities of JTP-74057 (GSK1120212), a novel MEK1/2 inhibitor, on colorectal cancer cell lines in vitro and in vivo. *Int. J. Oncol.* **39**, 23–31 (2011).
41. Yamaguchi, T., Kakefuda, R., Tanimoto, A., Watanabe, Y. & Tajima, N. Suppressive effect of an orally active MEK1/2 inhibitor in two different animal models for rheumatoid arthritis: a comparison with leflunomide. *Inflamm. Res.* **61**, 445–454 (2012).
42. Jing, J. P. et al. Comprehensive predictive biomarker analysis for MEK inhibitor GSK1120212. *Mol. Cancer Ther.* **11**, 720–729 (2012).
43. Varga, A. et al. A first-in-human phase I study to evaluate the ERK1/2 inhibitor GDC-0994 in patients with advanced solid tumors. *Clin. Cancer Res.* **26**, 1229–1236 (2020).
44. Blake, J. F. et al. Discovery of (S)-1-(4-chloro-3-fluorophenyl)-2-hydroxyethyl)-4-(2-((1-methyl-1H-pyrazol-5-yl)amino)pyrimidin-4-yl) pyridin-2(1H)-one (GDC-0994), an extracellular signal-regulated kinase 1/2 (ERK1/2) inhibitor in early clinical development. *J. Med. Chem.* **59**, 5650–5660 (2016).
45. Ohori, M., Takeuchi, M., Maruki, R., Nakajima, H. & Miyake, H. FR180204, a novel and selective inhibitor of extracellular signal-regulated kinase, ameliorates collagen-induced arthritis in mice. *Naunyn Schmiedebergs Arch. Pharmacol.* **374**, 311–316 (2007).

Acknowledgements

We thank Z. Liu from PKU for discussions on structural analysis. This work was supported by the National Key R&D Program of China (2018YFA0900200 to Z.X., 2017YFC1700402 to R.Z.), NSFC (31771519 to Z.X., 81873597 to H.Z., 81870590 to R.Z.) and the Beijing Municipal Natural Science Foundation (5182012 to Z.X.). The HUA and NASH studies were supported by Beijing Gigaceuticals Tech. Co, Ltd.

Author contributions

Z.X. (theory and algorithm); B.G., Miaomia Gao, J.W., J.L. and R.Z. (obesity); J.Z., J.W., X.W., X.S. and N.Z. (NASH); Mingjing Gao, L.W., Y.A., Z.H. and H.Z. (HUA); Z.X., MMiaomia Gao, Y.Y., W.K. and Z.L. (computation); Z.X., J.Z. and R.Z. wrote the paper; Z.X., R.Z., N.Z. and H.Z. co-supervised the teams of subprojects. Z.X. supervised all the teams and is the lead contact.

Competing interests

J.W., Mingjing Gao and Z.L. work for Beijing Gigaceuticals Tech. Co., Ltd.

Additional information

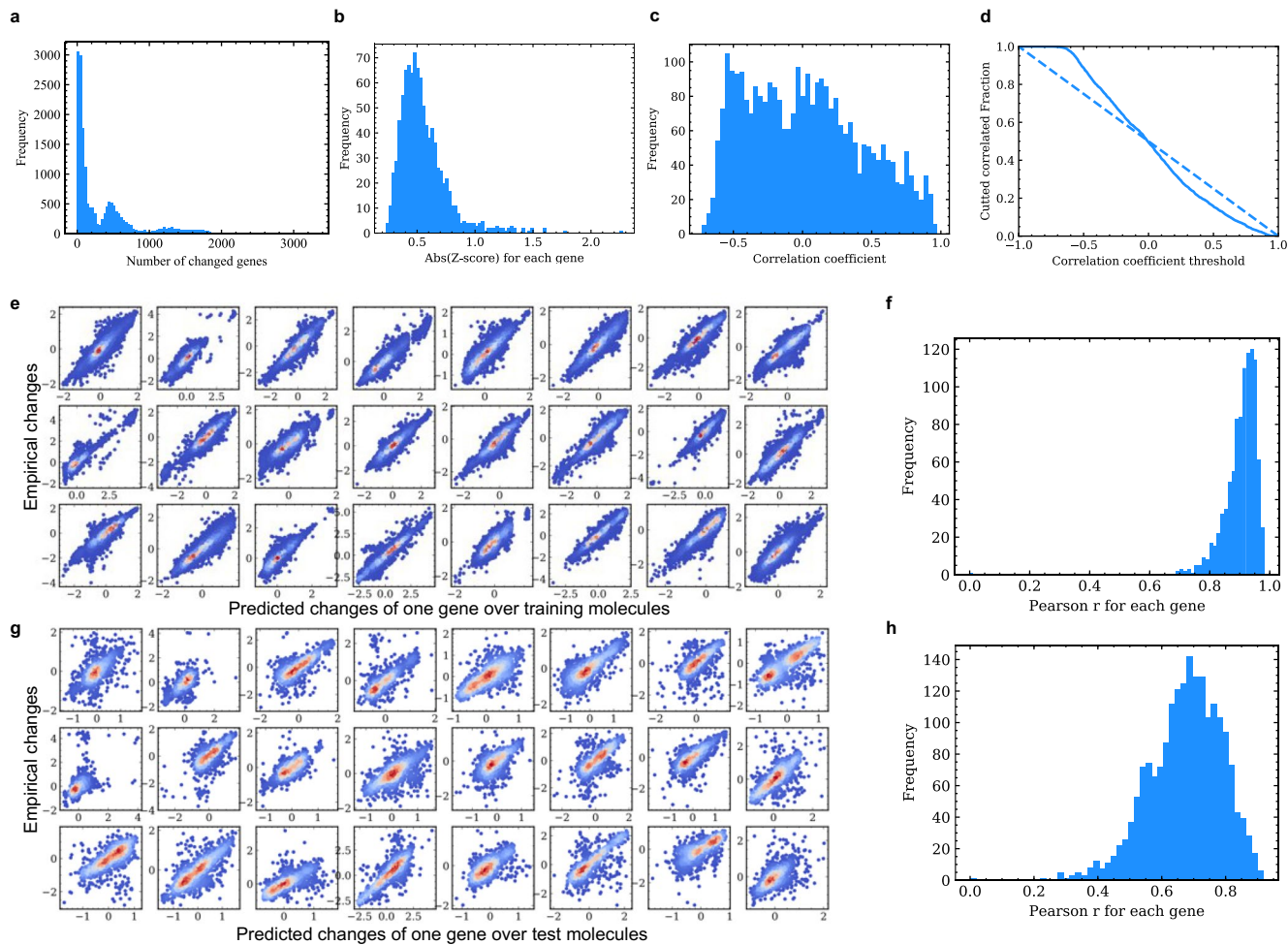
Extended data is available for this paper at <https://doi.org/10.1038/s41587-021-00946-z>.

Supplementary information The online version contains supplementary material available at <https://doi.org/10.1038/s41587-021-00946-z>.

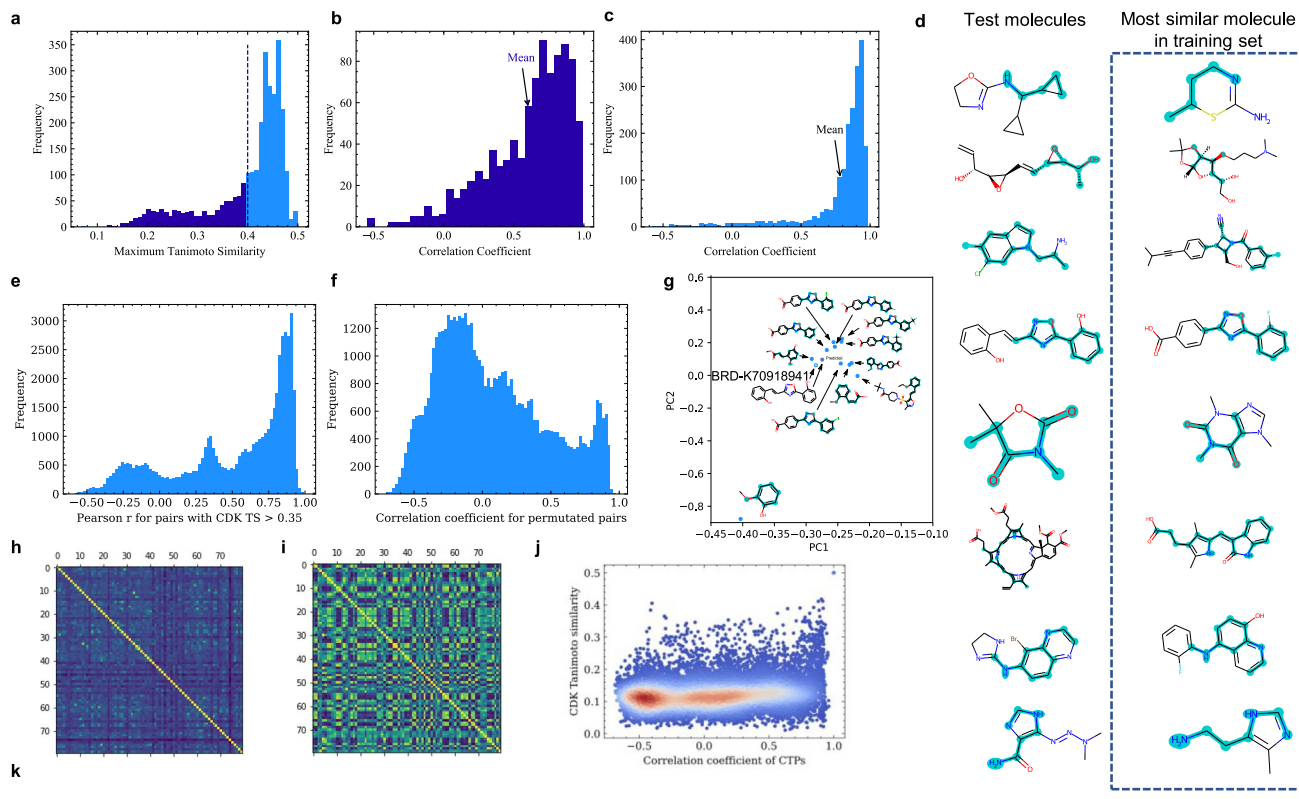
Correspondence and requests for materials should be addressed to H.Z., N.Z., R.Z. or Z.X.

Peer review information *Nature Biotechnology* thanks the anonymous reviewers for their contribution to the peer review of this work.

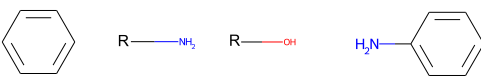
Reprints and permissions information is available at www.nature.com/reprints.



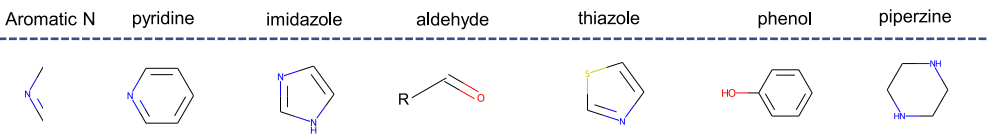
Extended Data Fig. 1 | Statistical analysis of the training data, control statistics and across-genes analysis. **a**, Distribution of number of changed genes for all molecules in L1000 data. **b**, Distribution of mean z-score across all genes for all molecules in L1000 data. **c**, As control, here shows the distribution of Pearson correlation coefficient r of randomly paired predicted profiles and empirical profiles. **d**, The ROC-like curve of well fitted fraction versus threshold Pearson r for distribution in **c**. **e, g**, The scatter plot of empirical versus predicted changes of one gene (each subplot) over all molecules (dots in each subplot) in training set (**e**) and test set (**g**). **f, h**, Distribution of Pearson correlation coefficient r of predicted and empirical profiles for genes over molecules in training set (**f**) and in test set (**h**).



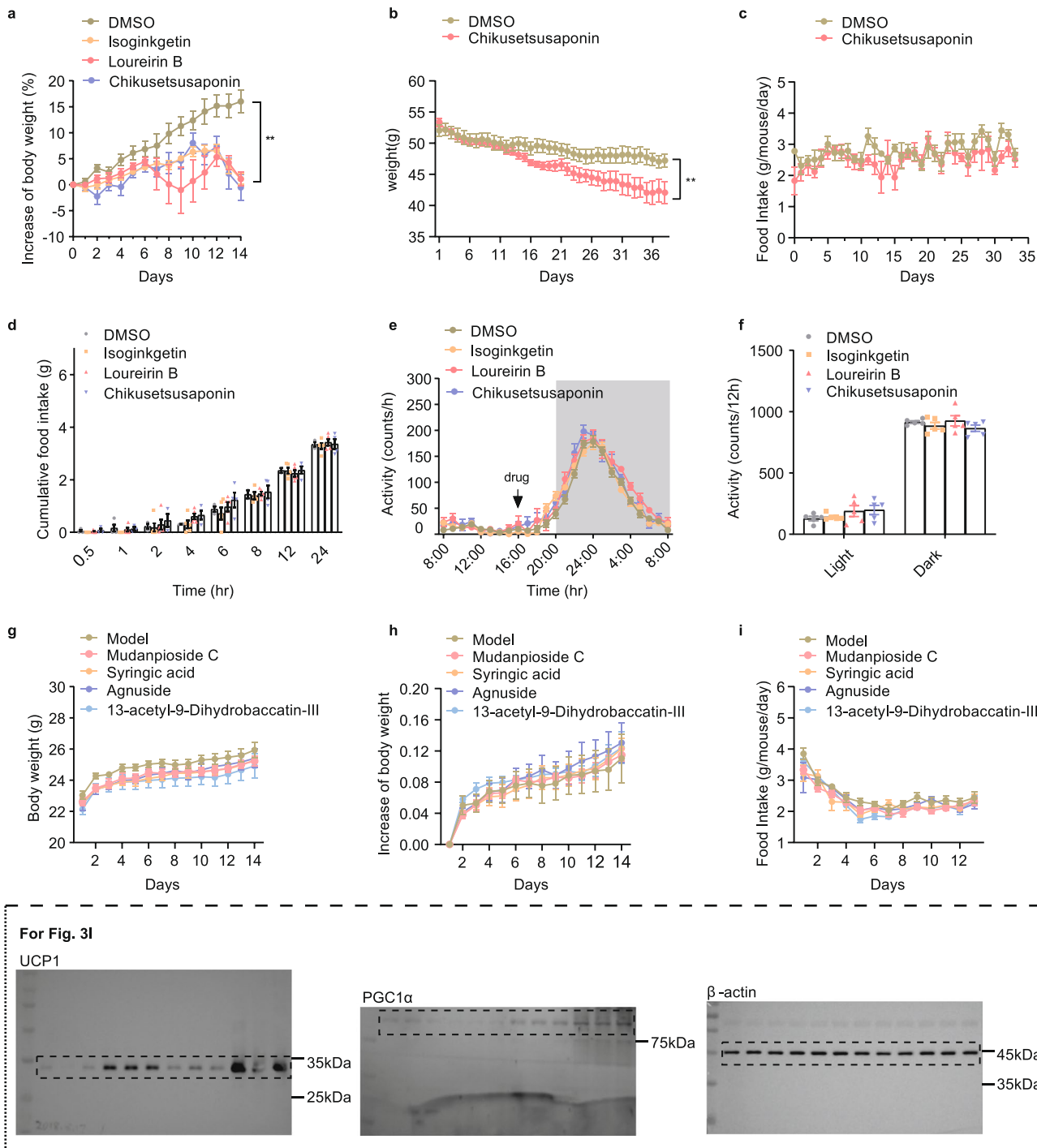
benzene -NH₂ aliphatic OH aniline sulfonamide trifluoromethyl amide



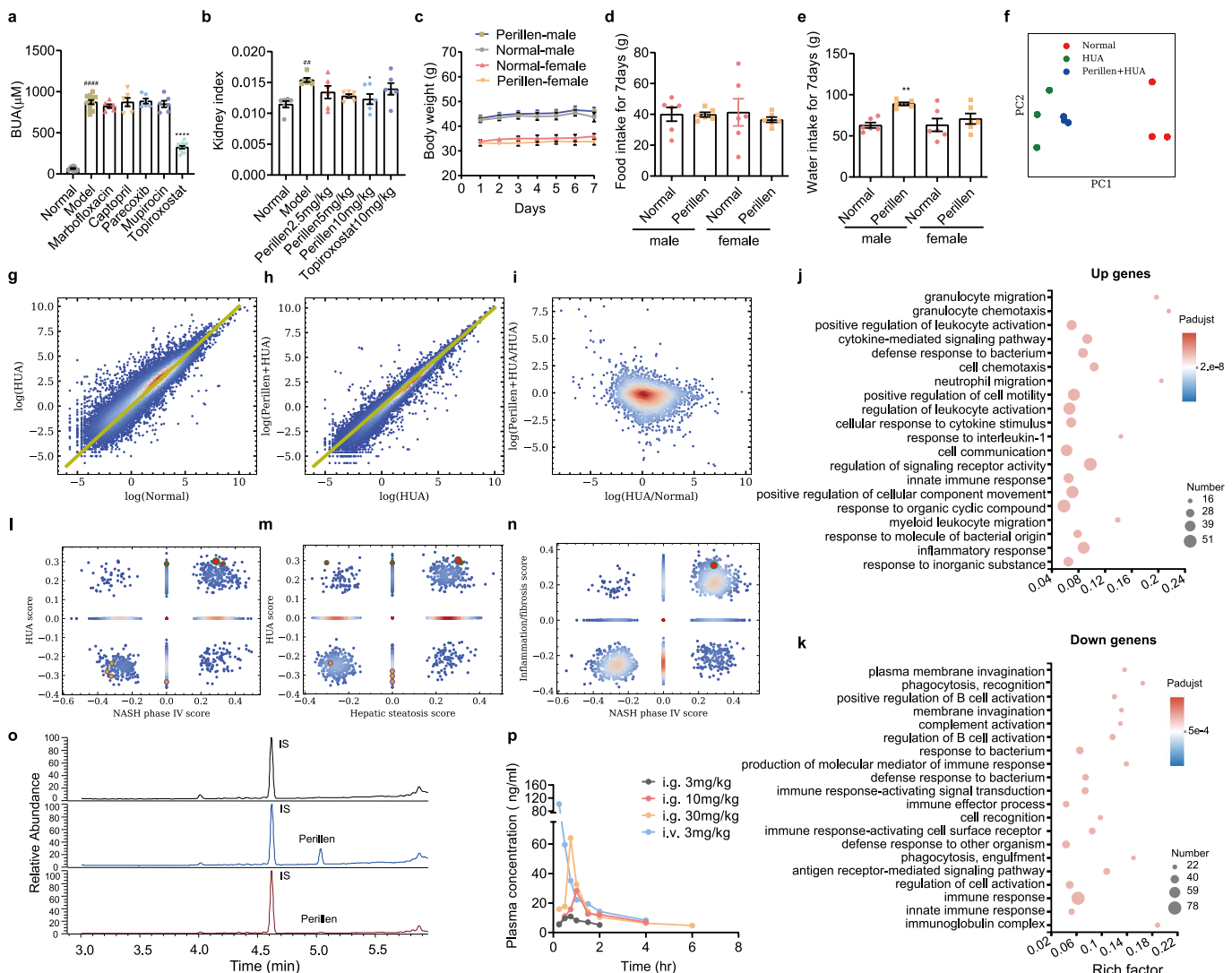
Exemplar fragments tend to disrupt (upper) and retain (bottom) the CTPs



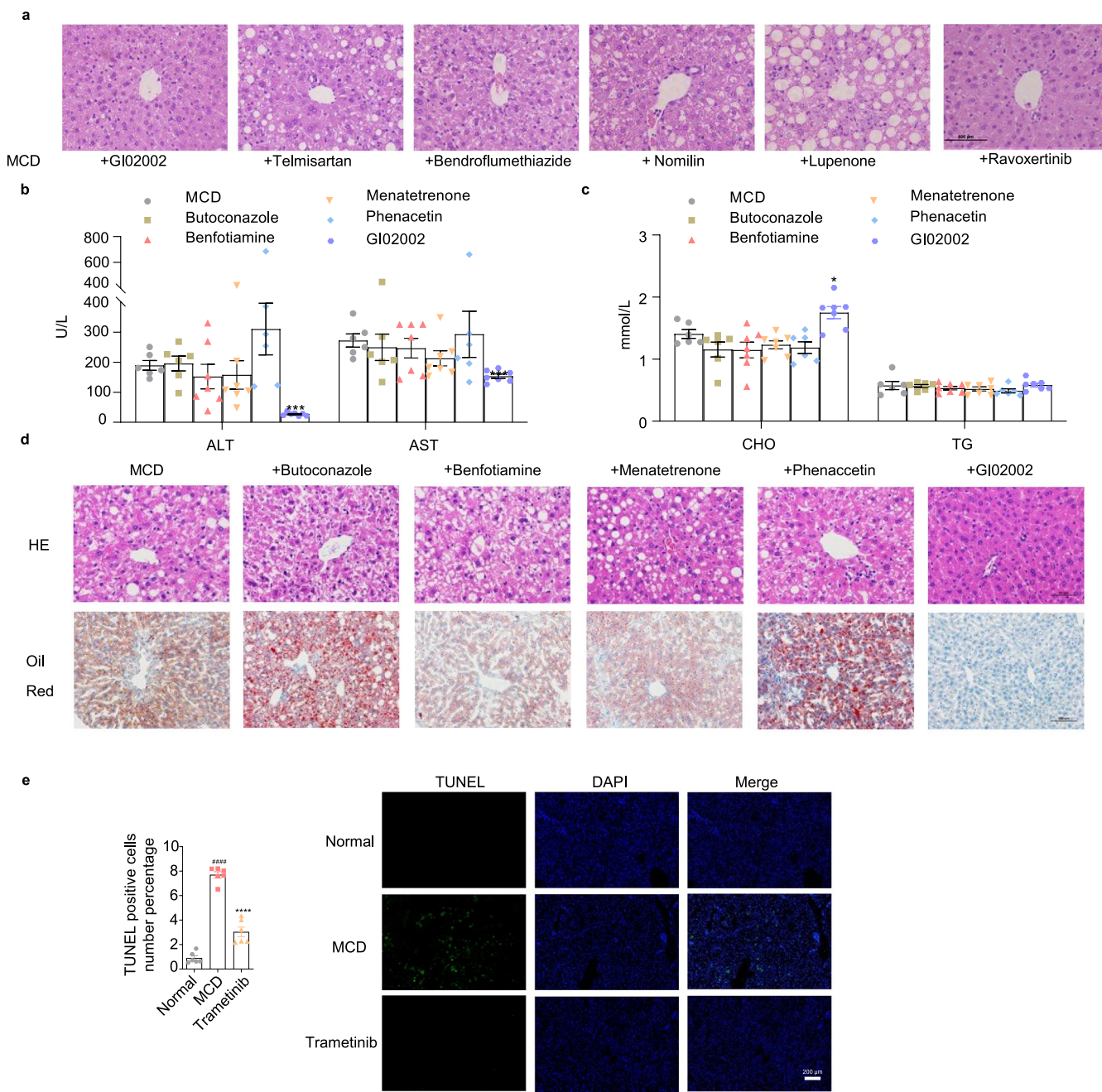
Extended Data Fig. 2 | Statistical and structural analysis of DLEPS' performance. **a**, The distribution of maximum Tanimoto Similarity based on CDK fingerprint (CDK TS) of each test molecule among comparison with all training molecules. **b, c**, The distribution of Pearson correlation coefficient r of predicted versus empirical changes of transcriptional profiles (CTPs) of test molecules with CDK TS < 0.4 (**b**) (mean $r = 0.60$, peak $r = 0.8$) and with CDK TS > 0.4 (**c**) (mean $r = 0.79$, peak $r = 0.93$). **d**, A few well-predicted test molecules ($r > 0.74$) and their most similar molecules in the training set, indicating DLEPS is capable of predicting CTPs of structurally novel molecules. The Maximum Common Sub-Structures (MCSS) are highlighted in cyan. **e**, The distribution of Pearson correlation coefficient r of predicted versus empirical CTPs among selected molecule pairs. One molecule in these pairs is from well-predicted test set ($r > 0.74$, $n = 2033$ out of 3000) and the other one in the pair is a structurally similar molecule from the training set, with CDK TS > 0.35 . The mean Pearson r equals to 0.50. **f**, As comparison, Pearson r for randomly permuted pairs equals to 0.07. **g–i**, Similarity versus correlation analysis of molecule pairs. **g**, Principal component analysis (PCA) of CTPs of test molecule BRD-K70918941 and its most similar molecules in training set. MCSS were highlighted in cyan for each molecule. DLEPS predicted CTP was highlighted in red. The heatmap of CDK Tanimoto similarity (**h**) and correlation coefficient matrix (**i**) of sampled pairs. **j**, Scatter plot of CDK TS versus correlation coefficient of CTPs, indicating that high CDK TS not necessarily yield high correlation and vice versa. **k**, The exemplar fragments tend to disrupt (upper) and retain (bottom) the CTPs, analyzed from the well ($r > 0.80$) / poorly ($-0.3 < r < 0.3$) correlated pair groups in **e**.



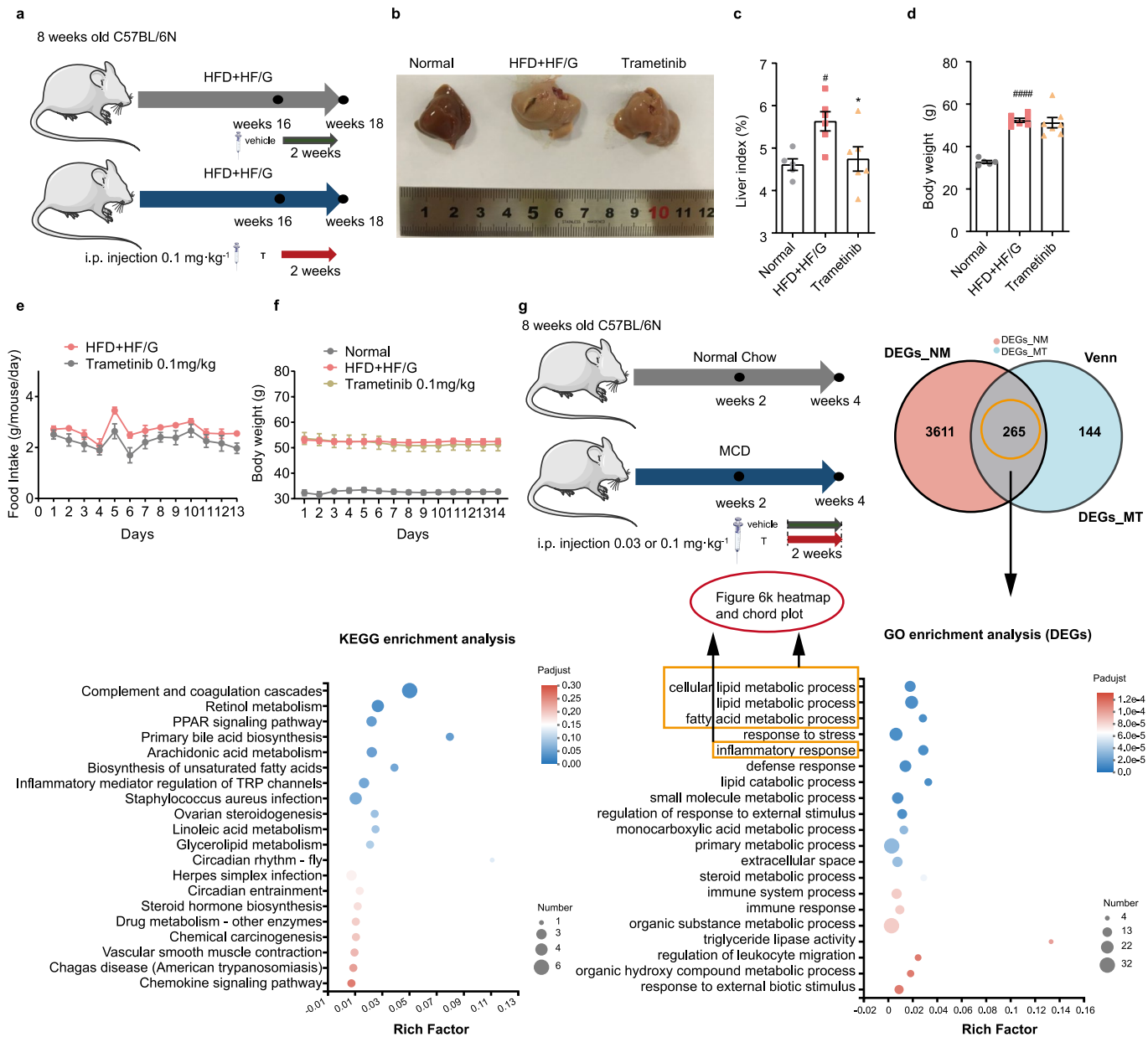
Extended Data Fig. 3 | Chikusetsusaponin IV reduced body weight in DIO mice and results of molecules from negative set. **a**, Increase of body weight ($n=6$) for 8 week-old mice that were housed at 22 °C, fed a HFD and treated with Isoginkgetin (3 mg/kg), Loureirin B (1 mg/kg), Chikusetsusaponin IV (20 mg/kg) or DMSO for 2 weeks. **b**, Body weight change of DIO mice that were treated by Chikusetsusaponin IV (20 mg/kg) continuously for 5 weeks. The average body weight at day 0 is 55 g in both groups ($n=6$). **c, d**, Daily and cumulative food intake ($n=6$) and **e, f** physical activity for mice in Fig. 3g-j. **g–i**, Body weight and food intake for molecules from negative set. Body weight **g**, increase of body weight **h** and food intake **i** ($n=6$) for 8 week-old mice that were housed at 22 °C, fed a HFD and treated with 4 molecules from negative set (Mudanpioside C 5 mg/kg, Syringic acid 25 mg/kg, Agnuside 5 mg/kg, 13-acetyl-9-Dihydrobaccatin-III 10 mg/kg or DMSO for 2 weeks). ** $P < 0.01$ compared with model group. All P values were determined by one-way ANOVA. All data are presented as the mean \pm sem.



Extended Data Fig. 4 | Transcriptional analysis of perillen treated mice, extra DLEPS analysis and pharmacokinetic analysis of perillen. **a**, Blood uric acid levels (BUA) of control, HUA model mice and HUA model mice treated with 4 molecules from negative set (Marbofloxacin, Captopril, Parecoxib and Mupirocin at 20 mg/kg, n=6). **b**, Kidney index of normal, HUA model mice and perillen treated HUA model mice at 2.5, 5 and 10 mg/kg and topiroxostat treated HUA model mice (n=6). **c**, Body weight (**d**) and water intake (**e**) of mice with treatment of perillen for 7 days (**c–e**, n=6). **f**, Principal component analysis of normal, HUA model, and HUA model perillen-treated mice (n=3). **g**, Scatter plot of gene expression in HUA model versus non-induced control mice. The color gradient represents dot intensity. **h**, Scatter plot of gene expression in perillen treated mice versus that of HUA model mice. **i**, Scatter plot of slopes in **h** versus that in **g** ($r = -0.23, P < 3e-232$). **j**, GO analysis of upregulated genes in model mice (n=3). **k**, GO analysis of downregulated genes in perillen treated model mice (n=3). **l–n**, Extra analysis of anti-inflammation and fibrosis score using a NASH phase IV gene signatures (**l**) and hepatic steatosis gene signatures (**m**). Big red dot highlights perillen, indicating prediction of perillen is robust to various inflammation/fibrosis gene signatures. **n**, Scatter plot of the inflammation/fibrosis score in Fig. 4b versus the NASH phase IV score ($r = 0.51, P < 2e-238$), indicating a well correlation of these two scores. **o**, Chromatograms of perillen. **p**, The serum concentration-time curves of perillen for 4 various conditions. * $P < 0.05$, ** $P < 0.01$, *** $P < 0.0001$ compared with model group. # $P < 0.01$, ##### $P < 0.0001$ compared with normal group (Normal). All P values were determined by two-tailed paired t-test. All data are presented as the mean \pm sem.



Extended Data Fig. 5 | Histological, serum and TUNEL analysis of molecules treated MCD model mice. 8 week-old mice were housed at 22°C, received MCD diets for two weeks, and then treated with positively predicted compounds: Normilin (6 mg/kg), Lupenone (2 or 6 mg/kg), Telmisartan (10 mg/kg), Bendroflumethiazide (1.5 mg/kg), GI02002 (10 mg/kg), Ravoxertinib (1mg/kg) in **a**, and with negatively predicted compounds: Butoconazole (10 mg/Kg), Benfotiamine (10 mg/kg), Menatetrenone (2.5 mg/kg), Phenacetin (70 mg/kg), GI02002 (10 mg/kg, positive control) or vehicle (0.5%CMC-Na containing 3%DMSO) in **b-d** by i.p. injection for 14 days. **a**, H&E (hematoxylin and eosin) staining of liver (3 mice replicates). **b**, Serum ALT and AST level ($n=6$ in MCD, Butoconazole and Phenacetin group, and $n=7$ in other groups, The P values of ALT in each group compared with model group were 0.8374, 0.4412, 0.5640, 0.1975 and 0.0002 respectively. The P values of AST in each group compared with model group were 0.6609, 0.5452, 0.1093, 0.8002 and 0.0002, respectively). **c**, Serum CHO and TG level ($n=6$ in MCD, Butoconazole and Phenacetin group, and $n=7$ in other groups, The P values of CHO in each group compared with model group were 0.1014, 0.1176, 0.0958, 0.0909 and 0.0177, respectively. The P values of TG in each group compared with model group were 0.8872, 0.5317, 0.4414, 0.2618 and 0.9238, respectively). **d**, H&E staining of liver (upper row, 3 mice replicates). Scale bar indicates 50 μ m. Oil-Red staining of liver (bottom row, 3 mice replicates). Scale bar indicates 100 μ m. **e**, Representative images of TUNEL staining (3 mice replicates, The P values model group compared with normal group were < 0.0001 and the P values Trametinib group compared with model group were < 0.0001, respectively). Scale bar indicates 200 μ m. All P values were determined by two-tailed paired t -test.* P < 0.05, ** P < 0.01, *** P < 0.001, **** P < 0.0001 compared with model group (MCD). ##### P < 0.0001 compared with normal group (Normal). All data are presented as the mean \pm sem.



Extended Data Fig. 6 | Support figures of HFD + HF/G experiments and transcriptional analysis of Trametinib treated mice. **a**, The schematic of administration protocol for Trametinib in HFD + HF/G-fed mice. **b**, The representative image of livers from different groups. **c**, The liver index for different groups ($n=5$ in normal group, $n=7$ in HFD + HF/G group, $n=6$ in Trametinib group). **d**, The mean body weight of different groups after treatment ($n=5$ in normal group, $n=7$ in HFD + HF/G group, $n=7$ in Trametinib group). The food intake (**e**, $n=7$ for each group) and the body weight (**f**) in different groups during drug administration. **g**, The schematic of administration protocol for Trametinib in MCD mice. KEGG and GO enrichment analysis of restored genes in Trametinib treatment. * $P < 0.05$ compared with model group. # $P < 0.05$, ##### $P < 0.0001$ compared with normal group (Normal). All P values were determined by one-way ANOVA. All data are presented as the mean \pm sem.

Reporting Summary

Nature Research wishes to improve the reproducibility of the work that we publish. This form provides structure for consistency and transparency in reporting. For further information on Nature Research policies, see our [Editorial Policies](#) and the [Editorial Policy Checklist](#).

Statistics

For all statistical analyses, confirm that the following items are present in the figure legend, table legend, main text, or Methods section.

n/a Confirmed

- The exact sample size (n) for each experimental group/condition, given as a discrete number and unit of measurement
- A statement on whether measurements were taken from distinct samples or whether the same sample was measured repeatedly
- The statistical test(s) used AND whether they are one- or two-sided
Only common tests should be described solely by name; describe more complex techniques in the Methods section.
- A description of all covariates tested
- A description of any assumptions or corrections, such as tests of normality and adjustment for multiple comparisons
- A full description of the statistical parameters including central tendency (e.g. means) or other basic estimates (e.g. regression coefficient) AND variation (e.g. standard deviation) or associated estimates of uncertainty (e.g. confidence intervals)
- For null hypothesis testing, the test statistic (e.g. F , t , r) with confidence intervals, effect sizes, degrees of freedom and P value noted
Give P values as exact values whenever suitable.
- For Bayesian analysis, information on the choice of priors and Markov chain Monte Carlo settings
- For hierarchical and complex designs, identification of the appropriate level for tests and full reporting of outcomes
- Estimates of effect sizes (e.g. Cohen's d , Pearson's r), indicating how they were calculated

Our web collection on [statistics for biologists](#) contains articles on many of the points above.

Software and code

Policy information about [availability of computer code](#)

Data collection

We used python pandas 0.24.2 for training and test data processing. The code for data processing are available at <https://github.com/kekegg/DLEPS>

Data analysis

The code for DLEPS are available at <https://github.com/kekegg/DLEPS>. We have also set up a user-friendly online computing interface (<https://www.dleps.tech/dleps/index>). Commercial use of DLEPS requires a license.

For manuscripts utilizing custom algorithms or software that are central to the research but not yet described in published literature, software must be made available to editors and reviewers. We strongly encourage code deposition in a community repository (e.g. GitHub). See the Nature Research [guidelines for submitting code & software](#) for further information.

Data

Policy information about [availability of data](#)

All manuscripts must include a [data availability statement](#). This statement should provide the following information, where applicable:

- Accession codes, unique identifiers, or web links for publicly available datasets
- A list of figures that have associated raw data
- A description of any restrictions on data availability

The training and test data for DLEPS have been downloaded from Gene Expression Omnibus (GEO) with accession number GSE92742. Browning markers, inflammation and fibrosis markers, NASH markers are analyzed from ArrayExpress (<https://www.ebi.ac.uk/arrayexpress/>) with accession number E-GEOID-8044, E-MEXP-980, E-GEOD-58979, respectively. All gene signatures were listed in Supp. Table 3. RNA-seq data for WAT from Chikusetsusaponin IV treated and control mice (GSE165171), kidney from perillen treated and control mice (GSE165173) and liver from Trametinib treated and control mice (GSE165174) were available at GEO (<https://www.ncbi.nlm.nih.gov/geo/>). These data were generated particularly for this study.

Field-specific reporting

Please select the one below that is the best fit for your research. If you are not sure, read the appropriate sections before making your selection.

Life sciences Behavioural & social sciences Ecological, evolutionary & environmental sciences

For a reference copy of the document with all sections, see nature.com/documents/nr-reporting-summary-flat.pdf

Life sciences study design

All studies must disclose on these points even when the disclosure is negative.

Sample size	We used DLEPS to predict effective drugs for diseases, we chose top ranked 3-6 compounds for animal tests. For mice models, we used >= 6 mice for experimental analysis. For RNA-seq, we used samples from 3 distinct mice.
Data exclusions	No data were excluded.
Replication	All attempts at replication were successful.
Randomization	Samples were randomly divided into groups.
Blinding	Samples were marked by one scientist and were blinded to another scientist for analysis.

Reporting for specific materials, systems and methods

We require information from authors about some types of materials, experimental systems and methods used in many studies. Here, indicate whether each material, system or method listed is relevant to your study. If you are not sure if a list item applies to your research, read the appropriate section before selecting a response.

Materials & experimental systems		Methods	
n/a	Involved in the study	n/a	Involved in the study
<input type="checkbox"/>	<input checked="" type="checkbox"/> Antibodies	<input checked="" type="checkbox"/>	ChIP-seq
<input type="checkbox"/>	<input checked="" type="checkbox"/> Eukaryotic cell lines	<input checked="" type="checkbox"/>	Flow cytometry
<input checked="" type="checkbox"/>	<input type="checkbox"/> Palaeontology and archaeology	<input checked="" type="checkbox"/>	MRI-based neuroimaging
<input type="checkbox"/>	<input checked="" type="checkbox"/> Animals and other organisms		
<input checked="" type="checkbox"/>	<input type="checkbox"/> Human research participants		
<input checked="" type="checkbox"/>	<input type="checkbox"/> Clinical data		
<input checked="" type="checkbox"/>	<input type="checkbox"/> Dual use research of concern		

Antibodies

Antibodies used	<p>β-ACTIN (ABclonal Technology, China, Catalog:AC026, Santa Cruz, sc-47778). STAT2 (Santa Cruz, sc-514193) UCP-1(abcam, ab10983) Goat polyclonal Secondary Antibody to Mouse IgG - H+L (Alexa Fluor® 488) (abcam, ab150113) HRP Goat Anti-Rabbit IgG (H+L) (ABclonal Technology, China, Catalog:AS014) HRP Goat Anti-Mouse IgG (H+L) (ABclonal Technology, China, Catalog:AS003)</p>
-----------------	--

Validation	<p>Stat2 (B-3) is a mouse monoclonal antibody specific for an epitope mapping between amino acids 7-26 at the N-terminus of Stat2 of human origin. Stat2 (B-3) is recommended for detection of Stat2 p113 of mouse, rat and human origin by Western Blotting (starting dilution 1:100, dilution range 1:100-1:1000), immunoprecipitation [1-2 µg per 100-500 µg of total protein (1 ml of cell lysate)], immunofluorescence (starting dilution 1:50, dilution range 1:50-1:500). UCP-1: Rabbit polyclonal to UCP1; Application: Use at a minimum dilution of 1/1000 in extract of rat brown adipose tissue (BAT) mitochondria or an extract of E.coli expressing recombinant mouse UCP1. Additional weak bands may be detected in some preparations of BAT extracts. Staining of the UCP1 band is specifically inhibited with the immunizing peptide. This antibody may not be suitable for Western blot in Human samples.</p>
------------	---

Eukaryotic cell lines

Policy information about [cell lines](#)

Cell line source(s)	State the source of each cell line used.
---------------------	--

Authentication

Describe the authentication procedures for each cell line used OR declare that none of the cell lines used were authenticated.

Mycoplasma contamination

Confirm that all cell lines tested negative for mycoplasma contamination OR describe the results of the testing for mycoplasma contamination OR declare that the cell lines were not tested for mycoplasma contamination.

**Commonly misidentified lines
(See ICLAC register)**

Name any commonly misidentified cell lines used in the study and provide a rationale for their use.

Animals and other organisms

Policy information about [studies involving animals](#); [ARRIVE guidelines](#) recommended for reporting animal research

Laboratory animals

In Obesity, C57BL/6 male mice (6-8 weeks, 18~22g) were obtained from the Department of Laboratory Animal Science of Peking University Health Science Center and the Charles River Laboratories Beijing Branch.
In NASH, C57BL/6 male mice (6-8 weeks, 18~22g) were obtained from the Charles River Laboratories Beijing Branch.
In Liquiritin, ICR male and female mice (6-8 weeks) were purchased from the Peking University Animal Department.
In Hyperuricemia, adult Kunming mice (8-week-old, 20~30 g, female, male) were provided by SPF (Beijing) Biotechnology.

Wild animals

The study did not involve wild animals.

Field-collected samples

Mice were housed under controlled light (12-h dark-light cycle, with the dark cycle encompassing 8 p.m. to 8 a.m), temperature (22±2°C) and humidity (50±10%) conditions with a free access to food and water.

Ethics oversight

All procedures in this study were carried out following the recommendations of the Guide for the Care and Use of Laboratory Animals of China Association for Laboratory Animals Science. All animal care protocols were approved by the Animal Care Committee of Peking University Health Science Center (Approval Number:LA2016113, LA2018189). All sacrifices were performed under pentobarbitone anesthesia, and every effort was made to minimize animal suffering.

Note that full information on the approval of the study protocol must also be provided in the manuscript.